Dear reviewers

Thank you so much for your time and effort in reviewing our paper. Please find our answers to your comments and the corresponding updates to the manuscript below. We hope to have addressed most of your comments which helped us improve the manuscript, and we will be happy to continue the discussion. At the end of this PDF, you can find the differences made to the manuscript with highlighted colors. In the coming days, we will submit the revised manuscript.

Emmanuel and co-authors

Reviewer 1

The paper addresses the “construction” of a digital twin for floating wind turbines that is verified against numerical simulations in a state-of-the-art offshore code and validated against real-world data. At present, the first commercial floating wind turbines are being installed and digital tools as the one presented in this article can be fundamental for their success. Therefore, the article is relevant to the international scientific community and falls within the scope of WES.

In general, the objectives and hypotheses of the article are clear. The methods are valid and can be reproduced by the reader, also thanks to the fact that the source code of the digital twin will be shared in a GitHub repository once the article will be published. The analyses presented by authors are valid and backed up by widely used simulations tools and previous research. Results are outlined in a clear way and the article is generally well structured in all its parts (text, figures, mathematics).

For all this reasons, the article deserves to be considered for publication in WES after being revised.

As a general comment, I see the tools presented in this article are derived from those developed in previous works about digital twins for bottom-fixed turbines. I suggest the authors to point out in the introduction the additional challenges of making a digital tool for a wind turbine with floating foundations. It may sound trivial, but I would explain why one cannot simply use tools derived for bottom-fixed turbines and where these are inaccurate.

>> Thank you for your comment, we have added the following paragraph in the introduction to highlight some of the challenges of the floating case:

"Developing digital twins for floating wind turbines present a set of challenges compared to our previous work on fixed-bottom foundations. The potentially large motions undergone by the platform may effect the aerodynamics and accelerometer signals. The models developed for fixed-bottom foundations need to be augmented to be able to predict the aerodynamics when the platform experiences large pitching motions. The dynamics of the platform motion needs to be well captured for the tower-top accelerometer to be used and for estimating the loading in the stationkeeping system. In both floating and fixed-bottom wind turbines, hydrodynamic loads need to be estimated to capture member-level loads in the substructure but they can be omitted as a first approximation if only the tower loads are estimated, as in this study."

Specific comments are reported below, and technical corrections are in the attached document.

Specific comments

102-103. The OpenFAST model is complemented with a closed-loop controller: is it based on a reference controller like ROSCO, are you allowed to give the reader some information about it?

The controller parameters are tuned so that OpenFAST simulations match SCADA data for selected operating conditions. Can you add something about the controller tuning?

>>> Thank you for your comment, we have modified the text as follows to give more details on the controller and its tuning:

"The OpenFAST model is complemented with NREL's Reference OpenSource Controller (ROSCO, Abbas et al. (2021)). The controller parameters are tuned so that OpenFAST simulations match the operating conditions of the turbine extracted from SCADA data (pitch, rotor speed and power). The nacelle velocity feedback option of ROSCO is used to reduce the platform pitching motion. Using trial and error, the frequency and damping ratio of the pitch PI-controller are set to ωp = 0.05 rad/s and ζp = 7\%, and the values for the torque controller are set ωQ = 0.15 rad/s and ζQ = 7\%. The gain-scheduling of the pitch controller are obtained using the tuning feature of ROSCO. We note that the controller is only needed to perform verifications of the digital twin with realistic time series of the turbine responses, but the controller itself is not used for the design of the digital twin."

l 109: why is it challenging?

>>> We have added the following to the text: "because the variations of the wind speed are sudden"

l 123

Can you say something more about the assumption of rotational symmetry of the platform? How do you think it might affect your study and its results?

>>> This is indeed a crude assumption. We have performed a sensitivity analysis on the mass and stiffness matrix and found that the assumption remained fair. We have added the following paragraph in the article

"Some of the consequences of this assumption is that we do no capture changes of inertial properties due to asymmetry of the support structure and changes of stiffness of the mooring system. In the case of the TetraSpar, the mass matrix of the floater does not vary significantly with the yawing of the coordinate system, and the assumption appears fair. We note that if the structure had perfect 120 \unit{deg} symmetry about the yaw axis, then its inertia would be invariant by yaw rotation. For the restoring stiffness of the mooring system, the diagonal terms do not vary significantly as the coordinate system yaws, but some of the coupling terms vary by 50\% to 200\%. The couplings between the platform degrees of freedom are likely wrongly estimated under the rotational symmetry assumption. The impact is nevertheless limited because most of the platform DOF (x, y,ϕ_x, and ϕ_y) are measured and therefore observable by the Kalman filter."

137-138. The capabilities of the Python code are not clear. If important for the rest of the study, I would explain better how the Python tools work and how it carries out the operations listed at lines 137-138

>>> Thank you for your comment, we have tried to reformulate the paragraph to highlight the features of the python code, and which ones are used.

"The WELIB approach consists of a set of dedicated open-source Python tools that are similar to the ElastoDyn, HydroDyn and MAP modules of OpenFAST. We developed these tools to offer additional modularity and granularity: the tools can be called individually or together; their states, inputs and outputs can be accessed and manipulated at each time step; and the structural dynamics equations are obtained analytically. For instance, this allows for: 1) analytical linearization of the structural dynamics, 2) simple linearization of the hydrodynamics (obtention of 6 × 6 matrices), 3) linearization of hydrodynamics with respect to wave elevation, 4) linearization with respect to parameters (Jonkman et al., 2022), and 5) interactive time-stepping of the linear and nonlinear model. In this work, we mostly use the first two features listed above and their usage will be described in Section 3.3.2. Results from time-stepping simulations will be presented in Section 3.3.3."

139-147. This paragraph does not convey adequately the difference between OpenFAST and WELIB. I understand that: 1) WELIB is somehow simpler (and less accurate?) than OpenFAST for nonlinear simulations 2) WELIB is easier to linearize and since it is based on an analytical approach it provides better understanding of the wind turbine physics.

I suggest the authors to work a bit on this paragraph to help the reader understand the complementarity of the two simulation tools with respect to the objectives of this study.

>>> Based on your multiple comments on this paragraph, we have tried to rewrite it. To make it clearer, we have split it into three parts: an overview, a description of WELIB tools, and a paragraph on the differences between the two.

Here are some excerpts of the rewritten paragraph:

Overview:

" In the next sections, we will show that the results from both approaches are consistent with each other so that either of the two can be used to obtain nonlinear and linear reduced order models. Ultimately, in Section 4, a mix of the two approaches is used for the digital twin: linear OpenFAST models for the state-space equations (Section 3.5) and WELIB for the virtual sensing step (Section 3.6)."

Comparison:

"Currently, no controller or aerodynamic module is present in WELIB. Therefore, nonlinear timestepping simulations with WELIB are limited to free-decay simulations or prescribed loads. Another shortcoming is that WELIB does not cover the full range of options available with OpenFAST, which is a continuously evolving, extensively verified and validated tool. Such options include the potential flow representation of hydrodynamic bodies, the flexibility of the floating structure, aerodynamic and control features. One benefit of WELIB over OpenFAST is the possibility to perform interactive time-stepping, that is, to change the states and inputs dynamically during the simulation. We do not use this approach in this work, but it can be considered for nonlinear digital twin applications, for instance, using an extended Kalman filter algorithm. Another benefit is the possibility to obtain analytical linear models of the structure, which avoids using finite-differences and therefore reduces the associated numerical errors. In the WELIB approach, the individual modules are linearized separately before being combined into the final linear model, and it is therefore easier to understand where each term in the Jacobians of the linear models comes from, and thereby, gain physical intuitiveness on the model. Ultimately, the linear models obtained by both approaches are similar and differ mostly based on differences in the structural dynamics equations and the implementation of rotational transformation matrices."

146, “to obtain analytical linear models and gain physical intuitiveness on the model”. From this sentence it's not clear the difference between a linear model obtained in WELIB and in OpenFAST. In the previous sentence it is said that WELIB can perform nonlinear simulations, so the difference for the linearized model is in how the model is obtained. I think you should briefly mention this issue and introduce what is explained in the next sections.

>>> Thank you for pointing this out, the models indeed mostly differ in how they are obtained. We hope that the rewritten paragraph clarifies this better.

169, “in two different ways”. It's not clear the added value of performing the linearization with Python and the HydroDyn module. I suggest the authors to focus on one of the two, or clarify why it is important to show in this study the results obtained with the two methodologies.

>>> Thank you for pointing that out. We have now rewritten this paragraph and tried to highlight the advantages and inconvenient of the different approaches. Obtaining the linearized hydrodynamic matrices is a question that often is asked by the OpenFAST community, and we therefore experimented with different approaches. The first one we tried (using full-system linearization) ended up being quite an involved process and somehow an important part of this work. We have therefore chosen to include it in this paper, as we do not think the approach is published elsewhere. The approach ended up being quite lengthy and prone to errors, which is why we turned to the other approach, simpler to implement and faster to run. We have tried to make the description less confusing in the updated version. The updated paragraph is as follows:

"We compute the 6×6 linearized rigid-body hydrodynamics matrices (mass matrix Mh, damping matrix Ch, and stiffness matrix Kh) corresponding to the six rigid-body motions of the platform. At the time of this study, these matrices could not be obtained directly from OpenFAST. While working on this issue, we ended up devising multiple ways to obtain them. They can now be obtained using: 1) full-system linearization of the HydroDyn module, 2) the Python implementation of the HydroDyn module by performing rigid-body perturbations of the full platform, or 3) an upgraded version of the OpenFAST HydroDyn driver that also uses rigid-body perturbations. The first approach uses baseline OpenFAST functionalities but requires additional postprocessing scripts and derivations. The full-system linearization of OpenFAST provides Jacobians of the hydrodynamic loads as a function of motions of the individual hydrodynamic analysis nodes (of which models often have hundreds to thousands of). To transfer these individual Jacobians to the reference point and obtain the 6×6 matrices, we developed and used the method presented in Appendix B. The process is involved and prone to errors. In comparison, the second and third approaches are straightforward to implement and are several orders of magnitude faster. The Python version was implemented first and then ported over to Fortran so that it can be readily available to the OpenFAST community. The consistency between the different approaches was verified, and because of its ease of use, the second approach is retained in this study. We note that in this study, all members are modeled using the Morison equation and the hydrodynamic drag is set to zero during the linearization process. There is therefore no frequency-dependent damping, and the effect of hydrodynamic drag is assumed to be part of the modeling uncertainty of the state estimator (see Section 3.5)."

180-181. Not clear what is Q0. I think you should rember that the degress of freedom of Mh are the platform motions which are only a subset of q. You should also recall the dimensions of Q0 and its structure.

>>> Additional details are now provided in the sentence: "The matrix Q0, of dimension 8 × 6, maps the subset of the 6 rigid-body platform degrees of freedom (x,y,z,φx,φy,φz), used for the definitions of Mh, Ch, Kh and Km, to the full vector of degrees of freedom, q."

3.3 Verification of the linear models. I suggest introducing this paragraph explaining why you used free decay simulations for verification of the linear models and no other types of simulation. Moreover, which is the purpose of simulations without hydrostatic restoring?

>>> Thank you for your comment, these are indeed valid points that we were explaining. We have added the following in the paragraph to justify the use of free-decay simulation:

"Free-decay simulations are sufficient because wave and aerodynamic loads are purposely not included in the linear models used by the digital twin. "

Further, to justify the use of simulations with hydrostatics, we have added the following:

"First, simulation without hydrodynamics (structure only) are considered, to isolate and verify the structural-dynamics part of the models."

l357 How did you get this information?

>>> This was indeed not clear. We performed sensitivity analyses (perturbing the mean platform pitch, tower fore-aft and thrust by +/- 5%) and looked at the relative changes in the section loads. We modified the text as follows:

"After performing a sensitivity analysis on the inputs and states of the system, we observed that the variables that most affect the fore-aft section loads are the platform pitch (ϕ_y), the tower fore-aft bending degree of freedom (q_t), and the aerodynamic thrust."

383, “adequate filtering of the input measurements can be used to tune the energy content at high frequencies”. Which is the impact of the frequency content above 1 Hz on fatigue loads? How meaningful it is compared to low-frequency harmonics? If you think they could be interesting, I suggest you add results of DEL obtained based on low-pass filtered signals.

>>> We believe there is quite some work to be done to further understand the differences of results between the DEL from the estimated signal and the reference signal. It seems that there is no easy way to get the DELs correctly because both low-frequencies and high-frequencies contribute to the DELs. For this paper, we prefer to point to our previous study, where indeed we showed that a tuned low-pass filter on the acceleration could lead to improvements in results. We have ideas on how this could be improved, but we would like to keep this for future work. We have added the following precision in the text: "As shown in previous studies, filtering of the input measurements can be used to tune the energy content at high frequencies. The method is yet unsatisfactory because it acts as an artificial rebalancing of energy content to achieve the desired DEL value. Both low and high frequency content contribute to the DEL values, therefore, we believe that systematic improvement is only possible through modeling improvements and higher observability of the states by the Kalman filter."

l 407: Can you give some numbers (min, max, mean)?

>>> We added the following precision in the text: "ranging from 4 to 24.5 \unit{m/s} with an overall mean of \unit{8.9} m/s."

421-422, “this is a crude first-order approximation”. Can you add some words about what you are neglecting using the tower top load cell?

>>> Thank you for your comment. We have added the following precision in parenthesis to mention some of the differences between the aerodynamic thrust and the load measured at the tower top: "e.g., neglecting inertial and gravitational loads, nacelle tilting and shaft bending."

428, “… or that the state estimator is failing”. Do you think that sensor issues can explain the different offset?

>>> You are correct, it could indeed be a source of error. We haven't found a clear explanation for the source of error. We have added the following in the text:

"Measurement errors could also affect the results, but no systematic error was detected over the time period investigated. It is therefore difficult to conclude as to what is the main source of error."

450, “gain-scheduling of the linear model, using nonlinear models”. You should briefly explain how these techniques can improve the results you already got.

>>> Thank you for your comment. We have now added small explanations in the list of potential improvements in our conclusion.

"Additional improvements could include:

1) gain-scheduling of the linear models to extend the domain of validity of the linear models used and reduce the modeling error,

2) using nonlinear models and extended Kalman filtering techniques to lift the linear assumptions that challenges the aerodynamics, hydrodynamics and structural dynamics,

3) etc. "

Reviewer 2

Digital twins for floating wind turbines is a topic of interest lately within the wind energy community. This paper addresses this subject in a clear and elegant way that is easy to follow. It starts by introducing the building blocks separately before combining everything together to obtain the digital twin tool. Afterwards, measurements from numerical simulations and full-scale data of the TetraSpar prototype are used for the validation of the tool. Not only that the tool is validated, but also, every component forming the digital twin is verified before validating the whole thing.

The paper reveals the potential gains the digital twins have to offer, which further promotes the wind energy scientific community. The methods and analyses performed are clear and valid, the scientific approach is clearly explained, which helps with the repeatability of the work. There is a good balance between the methods and the results with proper referencing.

The results are well presented and properly discussed till arriving at a well-drawn conclusion summarizing the work done. The abstract efficiently conveys the main message of the paper.

Accordingly, the paper meets the criteria of the journal and qualifies for publication after revision.

I see my fellow referee have many similar comments to mine. So, for brevity, I will add a few more:

Can you explain why you used a model of 8 DOFs in particular? Why not more?

>>> Thank you for your comment, we have now added a small paragraph to justify the choice of degrees of freedom:

"The selected set of DOF capture the first-order effects as it is the minimal set required to capture the full motion of the floater (necessary to compute restoring loads and tower loads), the tower flexibility (necessary to capture tower loads) and the rotor motion (necessary to capture the aerodynamics). Additional degrees of freedom could be considered to increase the modeling accuracy, e.g., to include floater flexibility for internal calculation of floater loads. This would increase the computational requirement and only contribute to second-order effects, and it is therefore postponed to future work. "

You mentioned that controller tuning was performed to match the SCADA data for OpenFAST simulations. What about the control system in WELIB? Does it use a wrapper like pHydrodyn but for ServoDyn? Can you elaborate on that a bit more?

>>> Thank you for pointing that out. The statement that nonlinear simulation with WELIB can be compared with OpenFAST could be misleading because no controller is currently implemented in WELIB. We have therefore added the following in the text:

"Currently, no controller or aerodynamic module is present in WELIB"

Lines 196-197, you mentioned that there exists a drift in the sway and roll responses, but you did not explain the reason for its existence. Can it be due to neglecting the hydrodynamic viscous term? Can it be the transformation matrix?

>>> Thank you for pointing this out. We do not have a "good explanation" for the drift. Free-decay simulations with less challenging initial conditions (smaller amplitudes) do no show such a drift, we therefore believe that the drift is mostly due to differences between linear and nonlinear models, which build up as you go away from the operating point. We have added the following at the end of the sentence: "which we assume can be attributed to inherent differences between linear and nonlinear models."

In Figure 4, there is an agreement in the peaks of the linear and nonlinear OpenFAST, while WELIB does not. Can you say something about that?

>>> We have revised this paragraph to further explain that the OpenFAST models are expected to be fully consistent (as they hit the same code base), whereas the difference between WELIB and OpenFAST linear are likely a propagation of the error in the yaw signal that couples to the other degrees of freedom.

"In all cases, the OpenFAST linear model is closer to the nonlinear OpenFAST model than the WELIB model. The consistency between the linear and nonlinear OpenFAST model is expected because they are obtained from the same code base. The WELIB linear model had difficulty capturing the yaw response. We believe that some of the error in the yaw signal is due to differences between the formulations of the three-dimensional rotations in OpenFAST and WELIB. The difference in yaw, results in a difference of coupling between the DOF, which can explain the differences observed in the sway, roll and rotor speed signals."

Line 389, can you cite a reference for the equations?

>>> There is no reference for these equations. A simple linear relationship was assumed based on the measurements at the given test site. We have modified the text to make this clearer:

"The H_s and T_p relationships were obtained by performing a linear regression on the sea state and wind measurements at the test site."

Line 451-452, "adding a model to account for wave excitation forces", can you elaborate a bit more what do you mean by this sentence? what would be the difference between this model and HydroDyn/ pHydrodyn?

>>> We have added the following paragraph higher up in the text when we discuss the hydrodynamic loads to clarify what we mean by "hydrodynamic model of the wave excitation force".

"In this work, δfh is mapped into the inherent model noise of the Kalman filter (see Section 3.5), but further improvements could be obtained by including a model for the wave-excitation loads. For instance, we could introduce a hydrodynamic state analog to the wave elevation or a set of states that scales different hydrodynamic shape functions so that the hydrodynamic load can be obtained as a linear superposition of scaled shape functions. In our application (tower section loads), such modeling did not appear necessary, but it will be considered in future work as it can be relevant to estimate substructure loads."

A final careful read should be done to brush off any spelling or grammatical mistakes.

>>> Thank you for your comment, we believe most of the spelling mistakes are now corrected.

Reviewer 3

This research focuses on the implementation of a physics-based digital twin solution for a floating offshore wind turbine, specifically the TetraSpar prototype. The digital twin aims to estimate aerodynamic loads, wind speed, and section loads along the tower to assess the fatigue lifetime of the structure. The solution incorporates a Kalman filter for structural state estimation, an aerodynamic estimator, and a physics-based virtual sensing procedure to obtain loads along the tower. The digital twin utilizes measurements commonly available on wind turbines and motion sensors typically used for floating platforms.

Two different approaches are explored to develop physics-based models: dedicated Python tools and the OpenFAST linearization feature, with a combination of both approaches in the final digital twin version. The OpenFAST linearization is for estimation of system states, and WELIB is used for sectional load calculations with the calculated states. Numerical experiments are conducted to verify the individual models, achieving estimated damage equivalent loads with an accuracy of 5% to 10% in simulation. When compared to measurements from the TetraSpar prototype, the errors increased to an average of 10%-15%. The results demonstrate promising accuracy and highlight the potential of digital twin solutions in estimating fatigue loads on floating offshore wind turbines.

Given the rise in popularity of digital twins for estimation of long term damage, I believe this article is fit for publication with minor adjustments and clarifications and will serve its purpose in continuing the progress of efficient digital twins for floating wind turbines.

For some general comments, I think the importance of computationally efficient digital twins should be highlighted and the computation time for each model should be evaluated, or explained.

Does OpenFAST compute fast enough for real time estimation?

If it doesn’t, is it possible to assume a significant increase in computational power would allow it to be run in real time?

>>> Thank you for your comment. You are right that the computational time is indeed crucial to achieve the goal of online estimations. To mention this earlier in the text, we have added the following to the introduction:

"Achieving computational efficiency is crucial to be able to run the digital twin online, therefore, a reduced order model with few selected degrees of freedom is used."

>>> In Section 4.2, we highlight the current computational time of the digital twin:

"The state estimation is currently 10 times faster than real time. The virtual sensing step is twice as fast as real time, but computational improvements are possible, in particular, by using a compiled language instead of Python."

>>> Currently OpenFAST cannot be used for real time estimations as it would require an interface where the inputs and states of OpenFAST can be modified at each time step. Yet, we agree with you that some

idea of the computational time for an OpenFAST simulation could give some perspective for the current work. The following was added in Section 4.2:

" For reference, OpenFAST simulations of the full TetraSpar model (with substructure flexibility) typically run 3 times slower than real time, and a reduced-order OpenFAST model with 8 degrees of freedom runs 1.1 times slower. Currently, real time estimation cannot be achieved with OpenFAST. Reduced-order modeling techniques, such as the ones presented in this article, are necessary to implement an online digital twin. Yet, if the digital twin is run as a postprocessing step, then parallelization using multiple CPUs could be used, e.g., processing different time periods of the day."

There are also questions on the hydrodynamic modeling of the floating platform. There seems to be an exclusion of the radiation damping of the platform. I assume this is due to the diameters relation to encountered wave lengths, but perhaps it would be helpful to explain this. If the platform is being modeled with Morrison's element, a brief discussion of this would be enlightening as well.

>>> Thank you for mentioning this. It is true that the original version of the manuscript was lacking details on the hydrodynamic modeling. We have added precisions at multiple places in the manuscript. In particular, we now explicitly mentioned the following:

"All the members of the substructure are modelled using the strip-theory approach (Morison equation) because the inherent long-wavelength assumption of the strip-theory approach has been shown to be sufficiently accurate for this structure with relatively slender members."

As a final statement about the hydrodynamics, what would be the effect of including wave excitation into the linearized model inputs, and why was this not used to begin with?

>>> You are correct that including wave excitation into the model could improve the modeling. It was our original intention to include it. OpenFAST currently cannot linearize with respect to wave elevation for strip-theory-based models, and one of the motivation for the python implementation pHydroDyn was to obtain such linear models. When scoping for this work and deciding to focus on tower loads, it appeared that including a wave model would not be as important because the tower loads are driven more by the wind input and platform motions (which are fairly well measured). We therefore postponed this to future work (mentioning "adding a model to account for wave excitation forces" in our future section of the conclusion). We do believe that improvements are possible by including a model for wave excitation. We believe that such modeling is important for fixed-bottom digital twins, or, for floating offshore digital twins that intend to determine substructure loads. We have added the following in the text:

"In this work, δfh is mapped into the inherent model noise of the Kalman filter (see Section 3.5), but further improvements could be obtained by including a model for the wave-excitation loads. In our application (tower section loads), such modeling did not appear necessary, but it will be considered in future work as it can be relevant to estimate substructure loads."

Comments/Questions:

29-30 : You mention the use of data driven models for digital twins, what are the strengths and weaknesses of these data driven models when compared to physics based? If any of these weaknesses led to the development of the physics based digital twin, it would be interesting to know.

>>> This is a fair point that we didn't highlight in the article. There are advantages and weaknesses to both approaches. We are now mentioning the main ones in the introduction:

"Machine-learning approaches can be trained using high-fidelity models or measurements, leading to potentially high accuracies while maintaining low computational time, but their training requirements imply that a technology cannot be readily transferred from one platform to another. Physics-based models often require low-fidelity models to achieve computational times low enough for digital twins to run in real time. They nevertheless offer the advantage that they provide tractable and insightful results, and they can be applied to a same family of wind turbine concepts because they do not require a training dataset. Currently, there is no definite case as to which approach can lead to the best digital twin implementation, and it is possible that future approaches will combine physics-based with data-driven techniques."

65-66: This is an important statement, as there are multiple definitions for digital twins so clarification is needed to the definition of digital twin in the scope of this article.

>>> Thank you for your comment, we hope that we made clear the definition we have in mind for this article in section 2.1

72: The goal is to use currently available measurements on the turbine (SCADA), but are there significant effects to adding more measurements? If the effect of adding more measurements to the physical turbine is positive enough, it may warrant a new addition of sensors to turbines in the field. The cost to add more sensors might be allowable if it can reduce the long term cost of the project with O&M decisions coming from digital twin estimations.

>>> Thank you for your comment, with which we strongly agree. The question of optimal placement and selection is outside the scope of this work, but we agree that it should be mentioned. We have taken some of your wording and added the following sentence in the paragraph:

"In this work, we leave open the question as to whether the installation of an additional set of optimally placed and selected sensors can further improve the predictions of the digital twin, further reducing the long-term O&M costs, and thereby warranting the additional costs of adding the sensors."

102: What values were tuned based on measurements?

>>> The OpenFAST model was implemented based on data provided by the partners. The controller was turned based on the SCADA measurements, and we have added the following sentences to provide more clarity on the controller tuning:

"The OpenFAST model is complemented with NREL’s Reference OpenSource Controller (ROSCO, Abbas et al. (2021)). The controller parameters are tuned so that OpenFAST simulations match the operating conditions of the turbine extracted from SCADA data (pitch, rotor speed and power). The nacelle velocity feedback option of ROSCO is used to reduce the platform pitching motion. Using trial and error, the frequency and damping ratio of the pitch PI-controller are set to ωp = 0.05 rad/s and ζp = 7\%, and the values for the torque controller are set ωQ = 0.15 rad/s and ζQ = 7\%. The gain-scheduling of the pitch controller are obtained using the tuning feature of ROSCO. We note that the controller is only needed to perform verifications of the digital twin with realistic time series of the turbine responses, but the controller itself is not used for the design of the digital twin."

The method for calculating excitation forces in the OpenFAST simulation is not apparent also.

>>> We have added the following sentence to clarify the modeling of the wave excitation force:

"All the members of the substructure are modelled using the strip-theory approach (Morison equation) because the inherent long-wavelength assumption of the strip-theory approach has been shown to be sufficiently accurate for this structure with relatively slender members.”

139: You mention WELIB has some shortcomings, but don’t mention what they are. These options could lead to discrepancies when comparing models. Are these limited options for structural dynamics, hydrodynamics, control?

>>> Thank you for your comment, which was also pointed out by the first reviewer. The main differences lay in the structural dynamics and choice of transformation matrices (when degrees of freedom introduce “rotations”). We have reworked the paragraph to attempt to add clarifications. In particular, we have added a paragraph highlighting the differences:

“Currently, no controller or aerodynamic module is present in WELIB. Therefore, nonlinear timestepping simulations with WELIB are limited to free-decay simulations or prescribed loads. Another shortcoming is that WELIB does not cover the full range of options available with OpenFAST, which is a continuously evolving, extensively verified and validated tool. Such options include the potential flow representation of hydrodynamic bodies, the flexibility of the floating structure, aerodynamic and control features. One benefit of WELIB over OpenFAST is the possibility to perform interactive time-stepping, that is, to change the states and inputs dynamically during the simulation. We do not use this approach in this work, but it can be considered for nonlinear digital twin applications, for instance, using an extended Kalman filter algorithm. Another benefit is the possibility to obtain analytical linear models of the structure, which avoids using finite-differences and therefore reduces the associated numerical errors. In the WELIB approach, the individual modules are linearized separately before being combined into the final linear model, and it is therefore easier to understand where each term in the Jacobians of the linear models comes from, and thereby, gain physical intuitiveness on the model. Ultimately, the linear models obtained by both approaches are similar and differ mostly based on differences in the structural dynamics equations and the implementation of rotational transformation matrices."

169-175: It is not explicitly stated which method was used.

>>> Thank you for pointing that out. We have now rewritten the paragraph describing the hydrodynamic linearization and we are now precise that the one used is the python rigid-body linearization.

“The consistency between the different approaches was verified, and because of its ease of use, the second approach is retained in this study. We note that in this study, all members are modeled using the Morison equation and the hydrodynamic drag is set to zero during the linearization process.”

192-194: This seems like a powerful use of the state-estimator, that is, to neglect forces and allow the estimator to account for the absence of these forces. To what degree is this valid?

>>> Thank you for this valid question. We have now tried to discuss the “degree of validity” and rationale in the text with the following addition:

“Assuming that the loading is part of the model noise is a crude approximation that is expected to be fair as long as the loading has a zero mean value, which is expected to be the case for the wave loading, but not for the wind or current loading (here omitted). This modeling choice is not very influential in this work because the motions of the platform measured by the inclinometers and GPS sensors inherently carry information about the wave loading."

322: You state the linear model is valid while close to the operating point. What is this region for a full scale turbine?

>>> This is a difficult question, and we haven't implemented gain scheduling to see if performance is improved with more linear models. We have added the following in the text:

"In this work, we used one operating point only and obtained results with fair accuracy (see Section 4). We nevertheless expect that to better represent the different operating regions of a pitch-regulated wind turbine, three to five linear models, stitched together through gain scheduling, would be needed."

356: The WELIB library is chosen for calculation of the sectional loads, but the full digital twin uses both WELIB and OpenFAST linearization. Is the job of OpenFAST linearized model to calculate the states of the system, while the WELIB calculates the section loads? If this is not the case, clarification is needed on the responsibility of each model.

>>> You are correct, after iterating on using either linear models from WELIB or OpenFAST we have now settled to use OpenFAST for the linear model. The comparison with WELIB is yet highly instructive as it can somehow give an "origin" for each of the numerical values found with OpenFAST because we have access to the analytical linear model, and the individual mooring and hydrodynamics matrices.

For the validation results, WELIB is only used for the "virtual sensing" step. We admit that this is confusing. The following paragraph was added early on (as soon as OpenFAST and WELIB are presented) to make it clearer to the reader.

" In the next sections, we will show that the results from both approaches are consistent with each other so that any of the two can be used to obtain nonlinear and linear reduced order models. Ultimately, in Section 4, a mix of the two approaches is used for the digital twin: linear OpenFAST models for the state-space equations (Section 3.5) and WELIB for the virtual sensing step (Section 3.6)."

A digital twin solution for floating offshore wind turbines validated using a full-scale prototype

Emmanuel Branlard[1], Jason Jonkman[1], Cameron Brown[2], and Jiatian Zhang [2]

[1]National Renewable Energy Laboratory, Golden, CO 80401, USA
[2]Stiesdal Offshore A/S, Denmark

Correspondence: E. Branlard (emmanuel.branlard@nrel.gov)

Abstract. In this work, we implement, verify, and validate a physics-based digital twin solution applied to a floating offshore wind turbine. The digital twin is validated using measurement data from the full-scale TetraSpar prototype. We focus on the estimation of the aerodynamic loads, wind speed, and section loads along the tower, with the aim ~~at~~ of estimating the fatigue lifetime of the tower. Our digital twin solution integrates ~~:~~ 1) a Kalman filter to estimate the structural states based on a linear model of the structure and measurements from the turbine, 2) an aerodynamic estimator, and 3) a physics-based virtual sensing procedure to obtain the loads along the tower. The digital twin relies on a set of measurements that are expected to be available on any existing wind turbine (power, pitch, rotor speed, and tower acceleration), and motion sensors that are likely to be standard measurements for a floating platform (inclinometers and GPS sensors). We explore two different pathways to obtain physics-based models: a suite of dedicated Python tools implemented as part of this work ~~, or~~ and the OpenFAST linearization feature. In our final version of the digital twin, we use components from both approaches. We perform different numerical experiments to verify the individual models of the digital twin. In this simulation realm, we obtain estimated damage equivalent loads with an accuracy of ~~the order of~~ approximately 5% to 10%. When comparing the digital twin estimations with the measurements from the TetraSpar prototype, the errors increased to 10%~~-~~–15% on average. Overall, the accuracy of the results ~~appears~~ is promising and demonstrates the possibility ~~to use~~ of using digital twin solutions to estimate fatigue loads on floating offshore wind turbines. A natural continuation of this work would be to implement the monitoring and diagnostics aspect of the digital twin ~~,~~ to inform operation and maintenance decisions. The digital twin solution is provided with examples as part of an open-source repository.

1 Introduction

The offshore floating wind turbine market is expected to grow in the ~~next~~ coming decades as the technology ~~is gaining~~ gains in maturity, with several floating wind turbine prototypes already tested and commissioned, such as the TetraSpar, developed by Stiesdal Offshore (Stiesdal Offshore, 2022). Operation ~~&~~ and maintenance (O&M) costs can account for approximately one-third of offshore wind farm life cycle expenditures for a fixed-bottom project and are expected to be higher for remote (floating) projects (Castella, 2020). Reducing the O&M costs is therefore an impactful and effective means to lower the costs of floating offshore projects. Digital twin solutions are increasingly being ~~considered~~ used to follow products during their life cycle to assess component conditions, guide predictive maintenance, and thereby reduce O&M costs. A review of digital twins for power systems is found in Song et al. (2023). Digital twins often include a virtual sensing component ~~, whose role consists of providing information that are~~ that provides information not measured by the physical system, and a structural health monitoring component to assess the condition of the system. Virtual sensing technology is usually achieved using physics-based or data-driven approaches; both approaches relying on measurements from the physical system to infer and extrapolate information about its current state. Physics-based approaches use a numerical model of the system, whereas data-driven approaches ~~either use ad-hoc~~ use either ad hoc algorithms or machine-learning techniques. Machine-learning approaches can be trained using high-fidelity models or measurements, leading to potentially high accuracies while maintaining low computational time, but their training requirements imply that a technology cannot be readily transferred from one platform to another. Physics-based models often require low-fidelity models to achieve computational times low enough for digital twins to run in real time. They nevertheless offer the advantage that they provide tractable and insightful results, and, they can be applied to a same family of wind turbine concepts because they do not require a training dataset. Currently, there is no definite case as to which approach can lead to the best digital twin implementation, and it is possible that future approaches will combine physics-based with data-driven techniques. This work presents the development, verification, and validation of a physics-based digital twin for floating wind turbines ~~,~~ as a proof of concept for future maturation of the technology.

Digital twins for wind turbine applications have recently become a topic of research interest. The ~~current~~ authors explored the topic of physics-based digital twins in previous work, ~~where~~ in which a method to estimate tower loads on land-based turbines was developed (Branlard et al., 2020a, b). The approach relied on a Kalman filter model (Kalman, 1960; Zarchan and Musoff, 2015) ~~,~~ that combines a linear physics-based model of the structure with measurements from the turbine to perform a virtual sensing of the tower section loads and estimate the fatigue of this component. The measurement data ~~was~~ were taken from the supervisory control and data acquisition (SCADA) system using sensors readily available on most turbines. The approach used a mix between an augmented Kalman filter approach (Lourens et al., 2012), where the loads are estimated with the states of the system, and a physics-based aerodynamic estimator for aerodynamic thrust. Bilbao et al. (2022) used a Gaussian process latent force model ~~instead~~ to estimate the forcing of the system ~~,~~ and thereby obtain the section loads along the tower. Drivetrains are another component ~~that has recently been an application of digital twin~~ for which a digital twin has been applied, with physics-based approaches presented ~~for instance in (Mehlan et al., 2022, 2023)~~in Mehlan et al. (2022, 2023), and data-driven models presented in Kamel et al. (2023).

~~In spite~~ Despite the recent popularity of the term “digital twin~~” becoming recently popular,it~~,” the concept is heavily based on the fields of ~~structural-health~~ structural health monitoring and load estimations (or more generally, virtual sensing), which have long been topics of research. For instance, Iliopoulos et al. (2016) used physics-based modal decomposition to estimate the dynamic response on the substructure of a fixed-bottom wind turbine. Neural networks have been used to establish transfer functions or surrogate models based on SCADA data to obtain wind turbine loads with the aim of performing conditional monitoring (see, e.g., Cosack (2010); Schröder et al. (2018)). Kalman filters were introduced in fields other than wind energy to perform load estimation~~, for instance in the following references: Auger et al. (2013); Ma and Ho (2004); Eftekhar Azam et al. (2015); Lourens et a~~ (Auger et al., 2013; Ma and Ho, 2004; Eftekhar Azam et al., 2015; Lourens et al., 2012). Kalman filtering has been extensively used in wind energy to estimate rotor loads and improve wind turbine control ~~, see, e. g.,Boukhezzar and Siguerdidjane (2011); Selvam et al~~ ~~.~~ (Boukhezzar and Siguerdidjane, 2011; Selvam et al., 2009; Bottasso and Croce, 2009; Bossanyi, 2003). Load estimations were also achieved using ~~hybrid-techniques~~ hybrid techniques combining physics based on SCADA data by Noppe et al. (2016). Other load estimation techniques may be used, such as lookup tables (Mendez Reyes et al., 2019), modal expansion (Iliopoulos et al., 2016), machine learning (Evans et al., 2018), neural networks (Schröder et al., 2018), polynomial chaos expansion (Dimitrov et al., 2018), deconvolution (Jacquelin et al., 2003), or load extrapolation (Ziegler et al., 2017).

In this work, we build on our previous work related to fixed-bottom turbines and present a digital twin solution for floating wind turbines that relies on physics-based models and a Kalman filter. We apply the digital twin to the TetraSpar structure and use measurements from the full-scale prototype. Achieving computational efficiency is crucial to be able to run the digital twin online, therefore, a reduced order model with few selected degrees of freedom is used. Developing digital twins for floating wind turbines present a set of challenges compared to our previous work on fixed-bottom foundations. The potentially large motions undergone by the platform may affect the aerodynamics and accelerometer signals. The models developed for fixed-bottom foundations need to be augmented to be able to predict the aerodynamics when the platform experiences large pitching motions. The dynamics of the platform motion needs to be well captured for the tower-top accelerometer to be used and for estimating the loading in the stationkeeping system. In both floating and fixed-bottom wind turbines, hydrodynamic loads need to be estimated to capture member-level loads in the substructure but they can be omitted as a first approximation if only the tower loads are estimated, as in this study.

In Section 2, we provide an overview of our digital concept, the vision for future application, and the TetraSpar prototype on which the digital twin is applied. In Section 3, we present the individual components of the digital twin, and run some isolated verification studies on them. In Section 4, we present results from the digital twin application first using numerical experiments, ~~and~~ then using measurements from the TetraSpar prototype ~~,~~ before concluding. To avoid lengthening the main text, we provide derivations (some ~~being~~ of which are important contributions of this work) and additional results in appendices.

2 Overview of the digital twin concept

In this section, we provide an overview of our digital twin concept and how it is applied in this study.

2.1 Long-term vision of the digital twin concept

Many definitions and applications of digital twins are possible. The vision for the concept discussed in ~~the~~ this work is to follow the life cycle of a wind turbine in ~~real-time~~ real time and ultimately provide tangible signals to inform O&M decisions. Our goal is to achieve this by relying only on measurements expected to be available on most wind turbines, thereby avoiding the extra cost of adding sensors. In this work, we leave open the question as to whether the installation of an additional set of optimally placed and selected sensors can further improve the predictions of the digital twin, further reducing the long-term O&M costs, and thereby warranting the additional costs of adding the sensors.

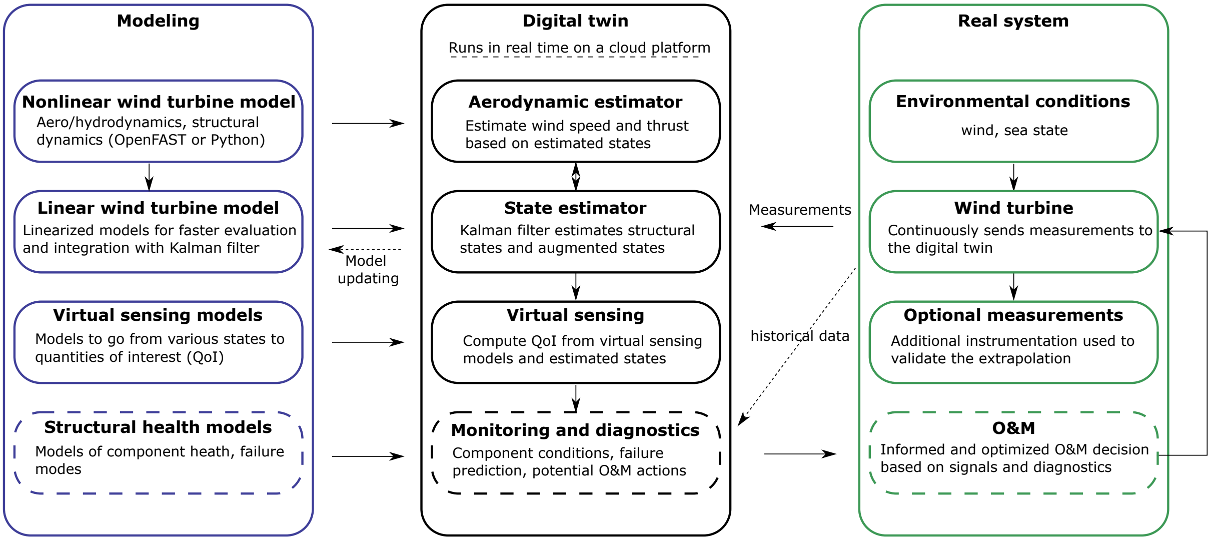
Modeling
Nonlinear wind turbine model
Aero/hydrodynamics, structural dynamics (OpenFAST or Python)
Linear wind turbine model
Linearized models for faster evaluation and integration with Kalman filter
Virtual sensing models
Models to go from various states to quantities of interest (QoI)
Structural health models
Models of component heath, failure modes
Model updating
Digital twin
Runs in real time on a cloud platform
Aerodynamic estimator
Estimate wind speed and thrust based on estimated states
State estimator
Kalman filter estimates structural states and augmented states
Virtual sensing
Compute QoI from virtual sensing models and estimated states
Monitoring and diagnostics
Component conditions, failure prediction, potential O&M actions
Measurements
historical data
Real system
Environmental conditions
wind, sea state
Wind turbine
Continuously sends measurements to the digital twin
Optional measurements
Additional instrumentation used to validate the extrapolation
O&M
Informed and optimized O&M decision based on signals and diagnostics

Figure 1. Overview of the digital twin concept. ~~Dashes~~ Dashed lines indicate features that are outside the current scope.

We illustrate our approach and vision in Figure 1. The digital twin is intended to run in ~~real-time~~ real time on a cloud platform. It combines a set of models (on the left of the figure) with data from the real system (on the right) to perform the estimation of various states and eventually produce diagnostics that can be use to inform the O&M. The data from the real system are taken from high-frequency measurements from the SCADA system (e.g., power, pitch, rotor speed). The states estimated by the digital twin include aerodynamic states (wind speed, thrust) and motions of the structure (e.g., surge, pitch, tower deflection). The core algorithm in the estimation is a Kalman filter that uses a linear wind turbine model. The estimated states are used in ~~an~~ a "virtual sensing" step ~~,~~ to produce quantities of interests (QoI), such as the loads at key locations of the structure. The QoI are then intended to be postprocessed by a monitoring and diagnostic tool to generate the data needed to perform condition-based O&M.

2.2 Narrowed scope

The boxes in Figure 1 ~~that are surrounded with dashes are not addressed in the current work, namely: the structural~~ with dashed-line borders—structural health modeling, monitoring and diagnostics, and O&M ~~decisions. These~~ decisions—are postponed to future work, even though they are essential steps ~~necessary~~ to achieve our final vision~~, but they are postponed to future work~~. Dashed lines ~~indicate possible~~ and arrows indicate options that may be exploited in the future but are also outside of our scope: the use of historical data to assist in the diagnostics, the use of estimates to perform ~~modeling~~ model updating, and real-time implementation.

This work therefore focuses on the estimation of states and environmental conditions under the assumption that the estimated quantities can replace costly measurements and eventually be used for O&M decisions. We intend to provide a proof of concept

~~paving~~ that paves the way for future commercial applications. A detailed description of each of the boxes surrounded with ~~plain lines will be provided~~ solid lines is given in Section 3.

2.3 System studied

2.3.1 The TetraSpar prototype

~~Throughout this article, the system studied~~ The system studied for this article is the TetraSpar floating offshore prototype. The system consists of a floating platform and ~~station keeping~~ stationkeeping system developed by Stiesdal Offshore in collaboration with partners Shell, RWE, and TEPCO Renewable Power, and a 3.6-MW wind turbine with a rotor diameter of 130 m developed by Siemens Gamesa Renewable Energy. A sketch of the system is provided in Figure 2. The prototype was installed off the coast of Norway and commissioned in November 2021. The prototype turbine is equipped with additional sensors (labeled “Optional measurements” in Figure 1), which we ~~will~~ use to validate the estimated QoI.

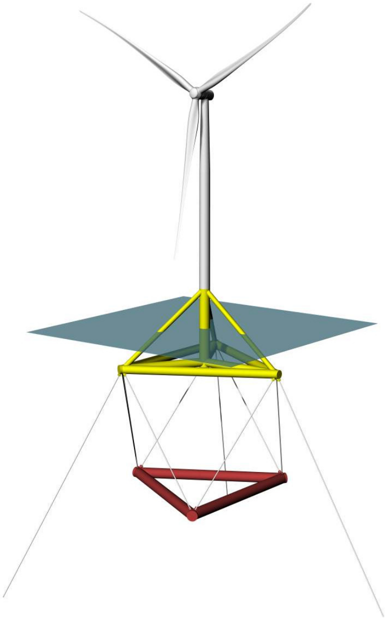

Figure 2. Sketch of the TetraSpar prototype

2.3.2 Numerical experiments

Prior to using measurement data, we ~~will~~ use simulations (referred to as “numerical experiments”) in place of the real system to ~~feed-in~~ feed data to the digital twin. The advantage of this approach is that the QoI are directly accessible and can be compared to the estimates for verification purposes.

Data for the numerical experiments ~~is~~ are obtained using OpenFAST simulations (Jonkman et al., 2023). A model of the TetraSpar floating platform and the wind turbine was implemented in OpenFAST based on data provided by the manufacturers. ~~The~~ All the members of the substructure are modelled using the strip-theory approach (Morison equation) because the inherent long-wavelength assumption of the strip-theory has been shown to be sufficiently accurate for this structure with relatively slender members. The OpenFAST model is complemented with NREL's Reference OpenSource Controller (ROSCO, Abbas et al. (2021)). The controller parameters are tuned so that OpenFAST simulations match the operating conditions of the turbine ~~were~~ extracted from SCADA data (pitch, rotor speed and power). The nacelle velocity feedback option of ROSCO is used to reduce the platform pitching motion. Using trial and error, the frequency and damping ratio of the pitch PI-controller are set to $\omega_p = 0.05$ rad/s and ~~a controller was tuned to approximate these conditions.~~ $\zeta_p = 7$ %, and the values for the torque controller are set $\omega_Q = 0.15$ rad/s and $\zeta_Q = 7$ %. The gain-scheduling of the pitch controller are obtained using the tuning feature of ROSCO. We note that the controller is only needed to perform verifications of the digital twin with realistic time series of the turbine responses, but the controller itself is not used for the design of the digital twin. We use the following modules of OpenFAST~~(see , and Jonkman et al. (2023))~~ (Jonkman et al., 2023): MAP (mooring lines), HydroDyn (hydrodynamics), ElastoDyn (tower and blade elasticity; rigid floater), AeroDyn (aerodynamics), InflowWind (wind inflow), and ServoDyn (controller interface).

For the numerical experiments, we use synthetic turbulent wind fields generated using TurbSim ~~(Jonkman and Buhl (2006))~~(Jonkman and Buhl, 2006). In particular, we ~~will~~ often use the same wind field, ~~that we will~~ which we refer to as the "turbulent step~~",~~," where a deterministic ramp and drop are added to a turbulent field. The advantage of this 10-min wind field is that ~~is~~ it covers all the operating regions of the turbine in a challenging way because the variations of the wind speed are sudden. The wind speed at hub height for the turbulent step can be seen in Figure 6.

2.3.3 Main aspects of the structural model

We model the structure using a set of 8 degrees of freedom (~~DOFs~~DOF), as illustrated in Figure 3. The platform is represented as a rigid body, and its motion is described using 6 ~~DOFs~~DOF: surge, sway, heave, roll, pitch, and yaw, respectively noted ~~$x, y, z, \phi_x, \phi_y, \phi_z$~~$x,\ y,\ z,\ \phi_x,\ \phi_y$, and ϕ_z. The tower bending in the fore-aft direction is represented using ~~one~~ 1 generalized DOF, q_t, associated with a Rayleigh-Ritz shape function, taken as the first fore-aft mode shape of the tower ~~(see, e. g., Branlard (2019)).~~ (Branlard, 2019). The shape function along the tower height, z_t, is written as $\Phi(z_t)$, with $\Phi(0) = 0$ at the tower bottom, and $\Phi(L_T) = 1$ at the tower top, where L_T is the tower length. The shaft rotation is noted ψ, so that the rotation speed of the rotor is $\dot{\psi}$~~where the dotted~~, where the dot notation indicates differentiation with respect to time. The ~~rotor-nacelle-assembly (RNA)~~ rotor-nacelle assembly is modeled as a rigid body. The full vector of ~~DOFs is therefore : $\boldsymbol{q} = [x, y, z, \phi_x, \phi_y, \phi_z, q_t, \psi]$~~DOF is therefore $\boldsymbol{q} = [x,\ y,\ z,\ \phi_x,\ \phi_y,\ \phi_z,\ q_t,\ \psi]$. The equations of motion will be recast into a first-order form by concatenating the vector of ~~DOFs~~ DOF and its time derivative~~:~~, $\boldsymbol{x} = [\boldsymbol{q}, \dot{\boldsymbol{q}}]$. The selected set of DOF capture the first-order effects as it is the minimal set required to capture the full motion of the floater (necessary to compute restoring loads and tower loads), the tower flexibility (necessary to capture tower loads) and the rotor motion (necessary to capture the aerodynamics). Additional degrees of freedom could be considered to increase the modeling accuracy, in particular to include

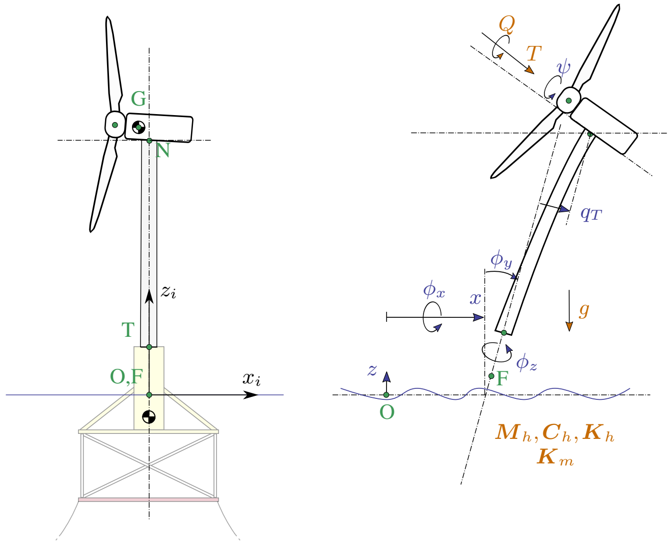

Figure 3. Notations for the structural modeling of the floating wind turbine, assuming no yawing of the nacelle. Left: main points (F, T, N, O, G) and inertial coordinate system (i). Right: degrees of freedom ($x, y, z, \phi_x, \phi_y, \phi_z, q_t, \psi$) and main loads: aerodynamics (T, Q), hydrodynamics (6 × 6 mass ~~,~~ and damping and stiffness matrices~~:~~, $\boldsymbol{M}_h$, $\boldsymbol{C}_h$, $\boldsymbol{K}_h$~~. Wave~~; wave excitation force neglected), mooring (6 × 6 stiffness matrix, $\boldsymbol{K}_m$), and gravity (g).

floater flexibility for internal calculation of substructure member loads. This would increase the computational requirement and only contribute to second-order effects, and it is therefore postponed to future work.

In this work, we perform ~~a~~ simplifying assumptions, e.g., neglecting the influence of nacelle yaw on the system. The measurement data ~~is~~ are conveniently provided in the fore-aft and side-side system of the nacelle. The main assumption is therefore that we assume a rotational symmetry of the platform and mooring system about the yaw axis. We intend to lift this assumption in future work. Some of the consequences of this assumption is that we do no capture changes of inertial properties due to asymmetry of the support structure and changes of stiffness of the mooring system. In the case of the TetraSpar, the mass matrix of the floater does not vary significantly with the yawing of the coordinate system, and the assumption appears fair. For the restoring stiffness of the mooring system, the diagonal terms do not vary significantly as the coordinate system yaws, but some of the coupling terms vary by 50% to 200%. The couplings between the platform DOF are likely wrongly estimated under the rotational symmetry assumption. The impact is nevertheless limited because most of the platform DOF (x, y,ϕ_x, and ϕ_y) are measured and therefore observable by the Kalman filter.

3 Individual components of the digital twin

In this section, we describe and verify the individual components of the digital twin presented in Figure 1. In Section 4, we ~~will~~ present applications of the digital twin where all the individual components are combined together.

3.1 Wind turbine measurements

The measurements used as inputs to the digital twin are listed in Table 1. These outputs are stored in a database at a sampling rate of 25 Hz. We expect these measurements to be standard sensors for any floating wind turbine. The TetraSpar prototype is equipped with additional measurements that ~~will be~~ are used to validate the implementation of the digital twin (see Section 4).

Table 1. Measurements used as inputs to the digital twin.

Signal	Symbol
~~Blade~~ Collective blade pitch angle	θ_p
Rotor speed	$\dot{\psi}$
Generator torque*	Q_g
~~Surge and Sway~~ Platform surge and sway	x, y
~~Roll and Pitch~~ Platform roll and pitch	ϕ_x, ϕ_y
Nacelle accelerations	$\ddot{\boldsymbol{r}}_N$

* Obtained from the power measurement using Equation 2.

3.2 Nonlinear wind turbine models

3.2.1 Overview

Similar to our previous work (Branlard et al., 2020b), we use two different pathways to obtain nonlinear and linear models of floating wind turbines: OpenFAST and WELIB (Wind Energy LIBrary, Branlard (2023b)). The ~~different modeling approaches are illustrated in~~ OpenFAST approach was described in Section 2.3.2, it is compared to the WELIB approach in Table 2 and ~~further presented below.~~ the WELIB toolset is further discussed below. In the next sections, we will show that the results from both approaches are consistent with each other so that either of the two can be used to obtain nonlinear and linear reduced order models. Ultimately, in Section 4, a mix of the two approaches is used for the digital twin: linear OpenFAST models for the state-space equations (Section 3.5) and WELIB for the virtual sensing step (Section 3.6).

~~The OpenFAST approach was described in . The~~

3.2.2 WELIB tools

The WELIB approach consists of a set of dedicated open-source Python tools that are similar to the ElastoDyn, HydroDyn and MAP modules of OpenFAST. We developed ~~this Python code~~ these tools to offer additional modularity and granularity~~, for instanceto allow for:~~: the tools can be called individually or together; their states, inputs and outputs can be accessed and manipulated at each time step; and the Python scripting eases the manipulation of the models. For instance, this allows for: 1) analytical linearization of the structural dynamics, 2) simple linearization of the hydrodynamics (obtention of ~~6x6~~ 6×6 matrices), 3) linearization of hydrodynamics with respect to wave elevation, 4) linearization with respect to parameters (Jonkman et al., 2022), and 5) interactive time-stepping of the linear and nonlinear ~~models. One shortcoming is that WELIB does not~~

Table 2. Approaches and tools used to obtain nonlinear and linear models.

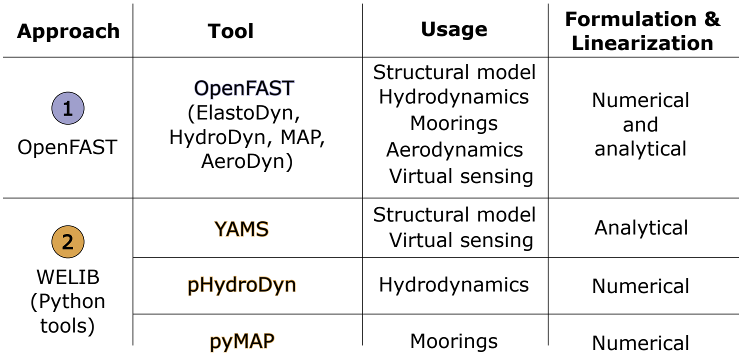

Approach	Tool	Usage	Formulation & Linearization
1 OpenFAST	OpenFAST (ElastoDyn, HydroDyn, MAP, AeroDyn)	Structural model Hydrodynamics Moorings Aerodynamics Virtual sensing	Numerical and analytical
2 WELIB (Python tools)	YAMS	Structural model Virtual sensing	Analytical
	pHydroDyn	Hydrodynamics	Numerical
	pyMAP	Moorings	Numerical

~~cover the full range of options available with OpenFAST, which is a continuously evolving, extensively verified and validated tool.~~ model. In this work, we mostly use the first two features listed above and their usage will be described in Section 3.3.2. Results from time-stepping simulations will be presented in Section 3.3.3. We expect to exploit the additional features of WELIB in future digital-twin implementations. For this work, we implemented the following tools in WELIB: 1) YAMS, a symbolic structural dynamics package to obtain the equations of motion of an assembly of rigid and flexible bodies analytically, and allow for their analytical linearization (Branlard and Geisler, 2022); 2) pHydroDyn, a Python version of the module HydroDyn (with a subset of HydroDyn's functionality) to determine the hydrodynamic loads; and 3) pyMAP, a wrapper around the MAP module of OpenFAST, to obtain the mooring quasi-statics. With these three additions, it is possible to perform nonlinear simulations of floating wind turbines using WELIB and perform comparisons with OpenFAST. ~~The benefits of~~

3.2.3 Differences between the two nonlinear approaches

Currently, no controller or aerodynamic module is present in WELIB. Therefore, nonlinear timestepping simulations with WELIB are limited to free-decay simulations or prescribed loads. Another shortcoming is that WELIB does not cover the full range of options available with OpenFAST, which is a continuously evolving, extensively verified and validated tool. Such options include the potential flow representation of hydrodynamic bodies, the flexibility of the floating structure, aerodynamic and control features. One benefit of WELIB over OpenFAST is the possibility to perform interactive time-stepping, that is, to change the states and inputs dynamically during the simulation. We do not use this approach in this work, but it can be considered for nonlinear digital twin applications, for instance, using an extended Kalman filter algorithm. Another benefit is the possibility to obtain analytical linear models ~~and~~ of the structure, which avoids using finite-differences and therefore reduces the associated numerical errors. In the WELIB approach, the individual modules are linearized separately before being combined into the final linear model, and it is therefore easier to understand where each term in the Jacobians of the linear models comes from, and thereby, gain physical intuitiveness on the model. ~~Results~~ Ultimately, the linear models obtained by both approaches are similar and differ mostly based on differences in the structural dynamics equations and the implementation of rotational transformation matrices. Results comparing time simulations using both approaches will be presented in ~~see~~ Section 3.3.

3.3 Linear wind turbine models

As part of our digital twin concept, we have chosen to use linear wind turbine models and a Kalman filter for the core of the state estimation (see Section 3.5). Nonlinear models and an extended Kalman filter could be considered in future iterations. In this section, we describe how the linear models from OpenFAST and WELIB are obtained.

3.3.1 OpenFAST linearization

OpenFAST can provide full-system linearization of its underlying nonlinear models by using a mix of ~~analytically- and finite difference-derived~~ analytically and finite-difference-derived Jacobians (Jonkman and Jonkman, 2016; Jonkman et al., 2018). The linearization process provides the state-space model ($\delta\dot{\boldsymbol{x}} = \boldsymbol{A}\delta\boldsymbol{x} + \boldsymbol{B}\delta\boldsymbol{u}$) and output equation ($\delta\boldsymbol{y} = \boldsymbol{C}\delta\boldsymbol{x} + \boldsymbol{D}\delta\boldsymbol{u}$) for small perturbations (indicated with δ) of the internal states ($\boldsymbol{x}$), inputs ($\boldsymbol{u}$), and outputs ($\boldsymbol{y}$) of OpenFAST, around ~~the linearized~~ a selected operating point. OpenFAST provides the linear model for the entire set of states, inputs, and outputs present in the model (including virtual sensor-type outputs typically written to an output file and not used internally). In this work, we extract subsets of the $\boldsymbol{A}$, $\boldsymbol{B}$, $\boldsymbol{C}$, and $\boldsymbol{D}$ matrices and combine them to form the linear model of the state estimator (see Section 3.5).

3.3.2 WELIB linearization

WELIB performs the linearization of the structure, hydrodynamics, and moorings independently ~~,~~ before combining them into one model. The aerodynamic loads are not linearized because a dedicated aerodynamic estimator is used in this work (see Section 3.4). The steps are as follows:

- The structural equations are linearized analytically using our symbolic framework (Branlard and Geisler, 2022). We ~~introduce~~ introduced a notion of “augmented inputs” to linearize the equations of motion without an explicit knowledge of the external forces. The process is described in Appendix A.

- We compute the 6×6 linearized rigid-body hydrodynamics matrices (mass matrix $\boldsymbol{M}_h$, damping matrix $\boldsymbol{C}_h$, and stiffness matrix $\boldsymbol{K}_h$) corresponding to the six rigid-body motions of the platform. ~~We obtain themusing numerical differentiation in two different ways~~At the time of this study, these matrices could not be obtained directly from OpenFAST. While working on this issue, we ended up devising multiple ways to obtain them. They can now be obtained using: 1) ~~using the~~ full-system linearization of the HydroDyn module, 2) the Python implementation of the HydroDyn module by performing rigid-body ~~perturbation~~ perturbations of the full platform, or ~~, 2) using~~ 3) an upgraded version of the OpenFAST HydroDyn driver that also uses rigid-body perturbations. The first approach uses baseline OpenFAST functionalities but requires additional postprocessing scripts and derivations. The full-system ~~linearization of the HydroDyn module. The latter~~ linearization of OpenFAST provides Jacobians of the hydrodynamic loads as a function of motions of the individual hydrodynamic analysis nodes (of which models often have hundreds to thousands of). To transfer these individual Jacobians to the reference point and obtain the 6×6 matrices, we developed and used the method presented in Appendix B. The process is involved and prone to errors. In comparison, the second and third approaches are straightforward to implement and are several orders of magnitude faster. The Python version was implemented first and then ported over to Fortran so that it can be readily available to the OpenFAST community. The consistency between the ~~two~~ different approaches was verified~~. The~~ , and because of its ease of use, the second approach is ~~not straightforward to implement, therefore, we upgraded the OpenFAST HydroDyn driver to provide the 6×6 hydrodynamic matrices directly without the need to use the full-system linearization .~~ retained in this study. We note that in this study, all members are modeled using the Morison equation and the hydrodynamic drag is set to zero during the linearization process. There is therefore no frequency-dependent damping, and the effect of hydrodynamic drag is assumed to be part of the modeling uncertainty of the state estimator (see Section 3.5).

- The linearized 6×6 mooring stiffness matrix, $\boldsymbol{K}_m$, is obtained by calling the linearization feature of the MAP module, and transferring the Jacobian to the reference point using the method outlined in Appendix B.

- The linearized equations of motion are assembled as:

$$[\boldsymbol{M}_0 + \boldsymbol{Q}_0\boldsymbol{M}_h]\,\delta\ddot{\boldsymbol{q}} + [\boldsymbol{C}_0 + \boldsymbol{Q}_0\boldsymbol{C}_h]\,\delta\dot{\boldsymbol{q}} + [\boldsymbol{K}_0 + \boldsymbol{Q}_0(\boldsymbol{K}_h + \boldsymbol{K}_m)]\,\delta\boldsymbol{q} = \delta\boldsymbol{f}_a + \delta\boldsymbol{f}_h \tag{1}$$

where the matrices with subscript 0 originate from the linearization of the structure (see Appendix A). The ~~term~~ matrix $\boldsymbol{Q}_0$ ~~is used here to map the~~ , of dimension 8×6, maps the subset of the 6 rigid-body platform ~~degrees of freedom~~ DOF $(x, y, z, \phi_x, \phi_y, \phi_z)$, used for the definitions of M_h, C_h, K_h and K_m, to the full vector of ~~degrees of freedom~~DOF, $\boldsymbol{q}$. The term $\delta\boldsymbol{f}_a$ is an approximation of the aerodynamic loads ~~,~~ and will be discussed in Section 3.4. The term $\delta\boldsymbol{f}_h$ is an approximation of the hydrodynamic wave-excitation loads~~and it will be~~ . In this work, $\delta\boldsymbol{f}_h$ is mapped into the inherent model noise of the Kalman filter ~~in~~ (see Section 3.5~~.~~). Assuming that the loading is part of the model noise is a crude approximation that is expected to be fair as long as the loading has a zero mean value, which is expected to be the case for the wave loading, but not for the wind or current loading (here omitted). This modeling choice is not very influential in this work because the motions of the platform measured by the inclinometers and GPS sensors inherently carry information about the wave loading. Improvements could be obtained by including a model for the wave-excitation loads, and further, limiting the wave load signal such that it remains within a certain frequency band.

For instance, we could introduce a hydrodynamic state analog to the wave elevation or a set of states that scales different hydrodynamic shape functions so that the hydrodynamic load can be obtained as a linear superposition of scaled shape functions. In our application (tower section loads), such modeling did not appear necessary, but it will be considered in future work as it can be relevant to estimate substructure loads.

- We recast Equation 1 into a first-order system to obtain the state matrix $\boldsymbol{A}$.

3.3.3 Verification of the linear models

In this section, we compare results from the OpenFAST nonlinear model, the OpenFAST linear model, and the WELIB linear model ~~,~~ for free-decay simulations of the TetraSpar structure. Free-decay simulations are sufficient because wave and aerodynamic loads are purposely not included in the linear models used by the digital twin. The OpenFAST linear model is obtained about the operating point defined by $\boldsymbol{q}_0 = \boldsymbol{0}$ and $\dot{\psi}_0 = 10\ \mathrm{rpm}$. All models (including the OpenFAST nonlinear model) use 8 ~~DOFs~~DOF. The initial conditions are set to ~~$\boldsymbol{q} = [1, -1, 0.6, 0.5, 0.5, 0, -0.2, 0]$~~ $\boldsymbol{q} = [1, -1, 0.6, 0.5, 0.5, 0, -0.2, 0]$ (in m and deg) and $\dot{\psi} = 10\ \mathrm{rpm}$, after which the structure is free to ~~decay~~move.

First, simulation without hydrodynamics (structure only) are considered, to isolate and verify the structural-dynamics part of the models. The time responses from the linear and nonlinear models are in strong agreement when only the structure is considered (see results in Appendix C). ~~Below, we present~~ Then, we consider results for a model that includes hydrodynamics ~~,~~ but without wind or external waves (still water). ~~Free decay of the structure using nonlinear and linear models for a case including moorings and hydrodynamics (still water). Time series of the main DOFs.~~We set the hydrodynamic drag to zero due to the difficulty in linearizing this term and ~~will~~ let the state estimator account for this modeling uncertainty. Results of the free-decay simulation are given in Figure 4 ~~,~~ for a time period of 153 s corresponding to the surge frequency. When

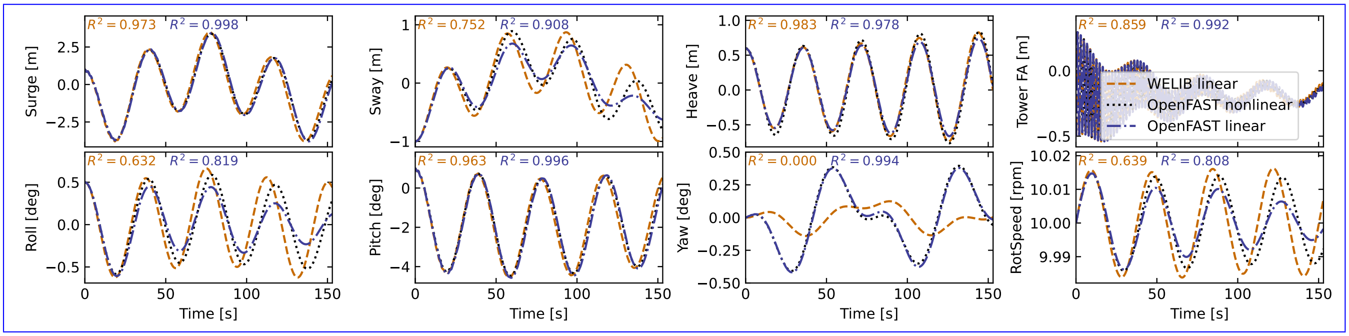

Figure 4. Free decay of the structure using nonlinear and linear models for a case including moorings and hydrodynamics (still water). Time series of the main DOF.

hydrodynamics is included, the time responses from the linear models are in strong agreement with the nonlinear OpenFAST results for the surge, heave, pitch, and tower fore-aft ~~DOFs~~DOF. The sway, roll, and rotor speed responses tend to drift as the simulation time advances~~. The WELIB linear model has difficulty capturing the yaw response. We believe that some of the error in the yaw signal is due to differences between the formulations of the three-dimensional rotations in OpenFAST and WELIB, resulting in a difference of coupling between the DOFs~~, which we assume can be attributed to inherent differences between linear and nonlinear models. The coefficient of determination (R^2) is indicated in Figure 4, comparing the linear models to the reference OpenFAST simulations for each response. In all cases, the OpenFAST linear model is closer to the nonlinear OpenFAST model than the WELIB model. The consistency between the linear and nonlinear OpenFAST model is expected because they are obtained from the same code base. The WELIB linear model had difficulty capturing the yaw response. We believe that some of the error in the yaw signal is due to differences between the formulations of the three-dimensional rotations in OpenFAST and WELIB. The difference in yaw, results in a difference of coupling between the DOF, which can explain the differences observed in the sway, roll and rotor speed signals.

To further quantify the differences between the models, we compare the natural frequencies obtained using the OpenFAST linear and WELIB linear models in Table 3. Overall, the frequencies between the two linear formulations agree very well (less ~~that~~ than 2.5% relative error), except for the roll frequencies (4% error) with hydrodynamics. Given the results of this section, we will continue this study using the OpenFAST linear model. We expect that continuous development of WELIB will further narrow the gap with OpenFAST in the future.

Table 3. Comparison of system frequencies obtained using the WELIB and OpenFAST linear models with and without hydrodynamics (no ~~addded~~ added mass, damping, hydrostatics, or wave excitation)

	Structure + mooring			**Structure + mooring + hydrodynamics**		
Mode	**OpenFAST [Hz]**	**WELIB [Hz]**	**Rel. Err [%]**	**OpenFAST [Hz]**	**WELIB [Hz]**	**Rel. Err [%]**
Surge	0.0088	0.0088	-0.2	0.0067	0.0065	-2.4
Sway	0.0088	0.0088	-0.1	0.0067	0.0068	0.7
Yaw	0.0163	0.0162	-1.0	0.0128	0.0128	-0.3
Pitch	0.0879	0.0886	0.7	0.0253	0.0257	1.6
Roll	0.0894	0.0902	0.9	0.0256	0.0266	4.0
Heave	NA	NA	NA	0.0276	0.0276	-0.2
Tower FA	0.5782	0.5789	0.1	0.5129	0.5145	0.3

3.4 Aerodynamic estimator

In Section 3.3, we indicated that the linear models were derived without accounting for aerodynamics. Instead, we choose to include the aerodynamic contribution separately within the digital twin. The reason for this choice is that the determination of the aerodynamic loads is essential to capturing the main loading and deflections of the structure, in particular the tower, and ~~,~~ the aerodynamic loads vary significantly over the range of operating conditions. Therefore, separating this contribution limits the need to obtain different linearized models for different operating conditions. We have successfully applied this approach in the past (Branlard et al., 2020a). In this work, we extend this approach to accommodate the floating wind application. The different elements of the aerodynamic estimator consist of ~~:~~ a torque estimator, aerodynamic maps, and a wind speed estimator.

3.4.1 Kalman filter for torque estimation

We assume that the power and rotor speed are reliable measurement signals, and we further assume that the generator torque (relative to the low-speed shaft) can be inferred from the power signal as:

$$Q_g = \frac{P}{\dot{\psi}} \frac{1}{n\eta_{\text{DT}}(\dot{\psi})} \tag{2}$$

where η_{DT} is the drivetrain (gearbox and generator) efficiency ~~,~~and n is the gear ratio. For the TetraSpar, $n = 1$, and we assume $\eta_{\text{DT}} = 1$. The dynamics equation of the drivetrain is modeled as:

$$J_{\text{DT}}\ddot{\psi} = Q - Q_g \tag{3}$$

where J_{DT} is the inertia of the drivetrain about the shaft axis. If we assume that the generator torque is a measurement, then an augmented Kalman filter (Lourens et al., 2012) can be used to estimate the aerodynamic torque Q, using the following state equation:

$$\begin{bmatrix} \dot{\psi} \\ \ddot{\psi} \\ \dot{Q} \end{bmatrix} = \begin{bmatrix} 0 & 1 & 0 \\ 0 & 0 & \frac{1}{J_{\text{DT}}} \\ 0 & 0 & 0 \end{bmatrix} \begin{bmatrix} \psi \\ \dot{\psi} \\ Q \end{bmatrix} + \begin{bmatrix} 0 \\ -\frac{1}{J_{\text{DT}}} \\ 0 \end{bmatrix} Q_g \tag{4}$$

A random walk approach is used for the evolution of the torque, that is, $\dot{Q} = 0$, and the Kalman filter adds further model noise to this equation. The measurement equation of the Kalman filter is:

$$\begin{bmatrix} \dot{\psi} \\ Q_g \end{bmatrix} = \begin{bmatrix} 0 & 1 & 0 \\ 0 & 0 & 0 \end{bmatrix} \begin{bmatrix} \psi \\ \dot{\psi} \\ Q \end{bmatrix} + \begin{bmatrix} 0 \\ 1 \end{bmatrix} Q_g \tag{5}$$

In the following, we ~~will~~ write $\hat{Q}$, the aerodynamic torque obtained using the method outlined above. We ~~will~~ present verification results in Section 3.4.4.

3.4.2 Aerodynamic maps

It is commonly accepted that the aerodynamic ~~performances~~ performance of a wind turbine mostly depends on the tip-speed ratio and the pitch angle of the blade. With compliant structures, the bending of the blade, the bending of the tower, and the motions of the floating platform (in particular, the platform pitch) will also affect the aerodynamic ~~performances~~performance. These motions are to a large extent a function of the mean wind speed. Therefore, we ~~suggest to tabulate the aerodynamic performances as~~ recommend tabulating the aerodynamic performance as a function of wind speed (U), rotor speed ($\dot{\psi}$), blade pitch (θ_p), and platform pitch ~~ϕ_y (~~(ϕ_y, assumed to be in the fore-aft direction). The power and thrust coefficients, respectively noted C_P and C_T, are precomputed using aeroelastic simulations in OpenFAST for a discrete set of values of the ~~4~~ four input parameters. In the simulations, the blade and tower elasticity are accounted for. To limit the number of simulations, only the points that are within reasonable proximity of the regular operating conditions of the wind turbine are computed. The 4D aerodynamic maps are precomputed as follows:

$$C_P(U,\dot{\psi},\theta_p,\phi_y), \quad C_T(U,\dot{\psi},\theta_p,\phi_y) \tag{6}$$

$$U \in \{2,3,\cdots,25\}\ \text{m.s}^{-1}, \quad \dot{\psi} \in \{5,5.5,\cdots,18\}\ \text{rpm}, \tag{7}$$

$$\theta_p \in \{-1,0,\cdots,30\}\ \text{deg}, \quad \phi_y \in \{-10,0,15\}\ \text{deg} \tag{8}$$

The precomputed values are stored in a database.

3.4.3 Wind speed estimation

The digital twin uses the aerodynamic map database to estimate the wind speed and aerodynamic thrust. For a given air density (ρ), rotor radius (R), and ~~given measurements $\dot{\tilde{\psi}}, \tilde{\theta}_p, \tilde{\phi}_y$~~measurements $\dot{\tilde{\psi}},\ \tilde{\theta}_p,\ \tilde{\phi}_y$, the aerodynamic torque and thrust are readily obtained as a function of wind speed from the database:

$$Q(U) = \frac{1}{2}\rho\frac{U^3}{\dot{\tilde{\psi}}}\pi R^2 C_P(U, \dot{\tilde{\psi}}, \tilde{\theta}_p, \tilde{\phi}_y), \qquad T(U) = \frac{1}{2}\rho U^2 \pi R^2 C_T(U, \dot{\tilde{\psi}}, \tilde{\theta}_p, \tilde{\phi}_y) \tag{9}$$

where ~~S.I.~~ SI units are assumed for all variables. For a given estimated torque ($\hat{Q}$), the estimated wind speed ($\hat{U}$) is found such that:

$$Q(\hat{U}) - \hat{Q} = 0 \tag{10}$$

As illustrated in Figure 5, multiple values of $\hat{U}$ can potentially satisfy Equation 10 because the aerodynamic torque is a nonlinear function of the wind speed. In such ~~case~~cases, we use the steady-state operating condition curve of the turbine to ~~chose~~ choose between the multiple solutions (typically two) ~~,~~ by selecting the point ~~that is~~ closest to this curve (see Figure 5). A relaxation scheme is also used, based on the previous estimate, to alleviate sudden jumps of the estimated wind speed.

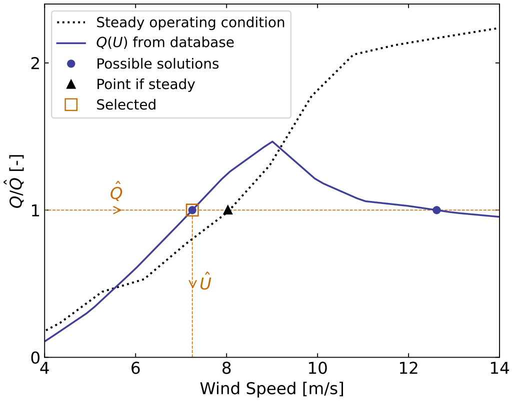

Figure 5. Illustration of wind speed estimation in the case where multiple wind speed values match the target torque value $\hat{Q}$

3.4.4 Verification of the aerodynamic estimator

To verify the aerodynamic estimator, we ran an OpenFAST simulation of the TetraSpar with the “turbulent step” wind field mentioned in Section 2.3.2 and irregular waves computed with a significant wave height of $H_s = 6$ m and a peak spectral period of $T_p = 14$, which represent a fairly extreme sea state for the site of the TetraSpar prototype. The simulated values of $\dot{\psi}$, θ_p, ϕ_y, Q_g are used as direct input to the aerodynamic estimator. Comparisons of the estimates with the OpenFAST outputs are shown in Figure 6. The shaded ~~area on the figure represent the area~~ areas on the graphs represent the areas where the generator torque is zero (turbine spinning up)~~, and~~ ; therefore, the wind speed estimator is not expected to work in that region. The ~~top~~

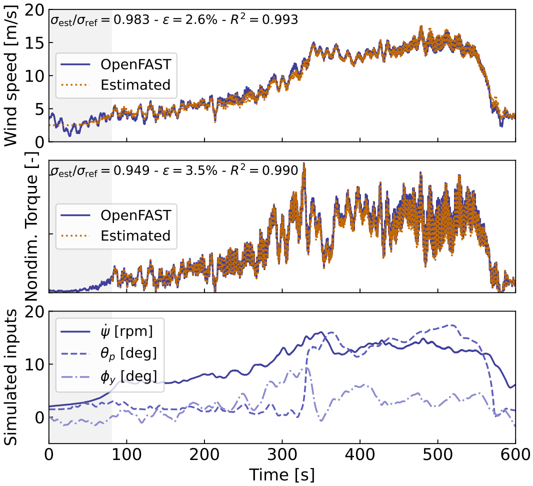

Figure 6. Example of aerodynamic estimation using "simulated measurements" from OpenFAST. Top: wind speed. Middle: Dimensionless torque. Bottom: structural inputs from the OpenFAST simulation provided to the estimator.

tops of the plots indicate the ratio of standard deviations, the mean relative error (ϵ), and the coefficient of determination (R^2). Throughout this article, we define the mean relative error of a quantity x as:

$$\epsilon(x) = \text{mean}_i \left[\frac{|x_\text{est}[i] - x_\text{ref}[i]|}{\text{mean}(|x_\text{ref}|)} \right] \tag{11}$$

where x_est is the estimated signal, x_ref is the reference signal, and $x[i]$ is the value of a signal at ~~the~~ time step i. Using the mean of $|x_\text{ref}|$ in the denominator avoids ~~issue~~ issues related to signals crossing 0. It results in lower mean relative error than if the instantaneous value ~~was~~ were used, but the metric is still indicative of how far the two signals are on average.

To quantify the performance of the estimator, we ~~reproduced~~ reproduce the simulation above, but ~~adding~~ add different noise levels to the measurements to account for measurement errors by the sensors. A Gaussian noise signal of zero mean and standard deviation $r\sigma$ is added to each input, where r is the noise level and σ is the standard deviation of the clean input. The results are shown in Table 4. As expected, the error in the estimation increases with increasing noise levels. This numerical experiment provides a rough quantification of the errors that can be expected from the aerodynamic estimator.

Table 4. Mean relative error (ϵ) of the wind speed, torque and thrust estimates ~~,~~ for increasing noise levels.

Noise level	0%	1%	5%	10%	20%
Wind Speed	2.6%	2.6%	3.1%	4.1%	6.7%
Torque	3.5%	3.8%	5.0%	6.8%	11.1%
Thrust	4.1%	5.1%	5.6%	7.3%	11.6%

3.5 State estimator

In this work, we follow a similar approach to our previous work ~~(e.g., Branlard et al. (2020a)),~~ (Branlard et al., 2020a), where an augmented Kalman filter is used to estimate states and loads. The Kalman filter used in the aerodynamic estimator (Section 3.4) is augmented with additional states and outputs. The Kalman filter uses two linear models: a state-equation, describing the time evolution of the states, and an output equation, describing how the measurements are related to the states and inputs. The state and output equations are written:

$$\delta\dot{\boldsymbol{x}}_{\text{KF}} = \boldsymbol{X}_x \delta\boldsymbol{x}_{\text{KF}} + \boldsymbol{X}_u \delta\boldsymbol{u}_{\text{KF}} + \boldsymbol{w}_x \tag{12}$$

$$\delta\boldsymbol{y}_{\text{KF}} = \boldsymbol{Y}_x \delta\boldsymbol{x}_{\text{KF}} + \boldsymbol{Y}_u \delta\boldsymbol{u}_{\text{KF}} + \boldsymbol{w}_y \tag{13}$$

where $\delta\boldsymbol{x}_{\text{KF}}$, $\delta\boldsymbol{u}_{\text{KF}}$, and $\delta\boldsymbol{y}_{\text{KF}}$ are the state, input, and output[1], respectively~~,~~; $\boldsymbol{X}_x$, $\boldsymbol{X}_u$, $\boldsymbol{Y}_x$, and $\boldsymbol{Y}_u$ are the system matrices that relate the different system vectors~~,~~; and, $\boldsymbol{w}_x$ and $\boldsymbol{w}_y$ are Gaussian processes represented modeling noise. The output vector, $\delta\boldsymbol{y}_{\text{KF}}$, is also referred to as the "measurement" vector ~~,~~because it corresponds to the measured signals. At a given time step, the Kalman filter algorithm uses the system matrices, a set of measurements, and an ~~a-priori~~ a priori knowledge of the model and measurement uncertainties to estimate the state vector (Kalman, 1960; Zarchan and Musoff, 2015).

In this work, we design the state estimator such that the state vector contains the structural degrees of freedom ($\delta\boldsymbol{q}$ and $\delta\dot{\boldsymbol{q}}$) and the aerodynamic torque ($\boldsymbol{Q}$), and the input vector consists of the thrust (obtained with the aerodynamic estimator) ~~,~~and the generator torque (obtained from the power). These design choices were guided by our previous work on the topic. For this choice of state and input variables, we build linear models for the state and output equations. We use the linear models described in Section 3.3 (the $\boldsymbol{A}$, $\boldsymbol{B}$, $\boldsymbol{C}$, $\boldsymbol{D}$ matrices) ~~,~~to populate the system matrices of the Kalman filter. ~~We provide additional~~ Additional details on how the relevant Jacobians are extracted are given in Section 3.6.1. Given our choice of system vectors, the state equation is:

$$\begin{bmatrix} \delta\dot{\boldsymbol{q}} \\ \delta\ddot{\boldsymbol{q}} \\ \dot{Q} \end{bmatrix} = \begin{bmatrix} \boldsymbol{0} & \boldsymbol{I} & \boldsymbol{0} \\ \boldsymbol{A}_{12} & \boldsymbol{A}_{22} & \frac{\partial\ddot{\boldsymbol{q}}}{\partial Q} \\ \boldsymbol{0} & \boldsymbol{0} & \boldsymbol{0} \end{bmatrix} \begin{bmatrix} \delta\boldsymbol{q} \\ \delta\dot{\boldsymbol{q}} \\ Q \end{bmatrix} + \begin{bmatrix} \boldsymbol{0} & \boldsymbol{0} \\ \frac{\partial\ddot{\boldsymbol{q}}}{\partial Q_g} & \frac{\partial\ddot{\boldsymbol{q}}}{\partial T} \\ 0 & 0 \end{bmatrix} \begin{bmatrix} Q_g \\ T \end{bmatrix} + \boldsymbol{w}_x \tag{14}$$

where ~~,~~ $\boldsymbol{A}_{\boldsymbol{12}}$ and $\boldsymbol{A}_{22}$ are the two lower blocks of the $\boldsymbol{A}$ matrix, and $\boldsymbol{I}$ is the identity matrix. The Jacobians with respect to the loads are extracted from the $\boldsymbol{B}$ and $\boldsymbol{D}$ matrices. A random walk approach is used for the evolution of the torque Q (that is, we set $\dot{Q} = 0$). The output equation, which effectively relates the measurements to the system states and inputs, is set as:

$$\begin{bmatrix} \delta\tilde{\boldsymbol{q}} \\ \dot{\psi} \\ \ddot{\boldsymbol{r}}_N \\ Q_g \end{bmatrix} = \begin{bmatrix} \frac{\partial\tilde{\boldsymbol{q}}}{\partial\boldsymbol{q}} & \frac{\partial\tilde{\boldsymbol{q}}}{\partial\dot{\boldsymbol{q}}} & \frac{\partial\tilde{\boldsymbol{q}}}{\partial Q} \\ \boldsymbol{0} & \tilde{\boldsymbol{I}} & 0 \\ \frac{\partial\ddot{\boldsymbol{r}}_N}{\partial\boldsymbol{q}} & \frac{\partial\ddot{\boldsymbol{r}}_N}{\partial\dot{\boldsymbol{q}}} & \frac{\partial\ddot{\boldsymbol{r}}_N}{\partial Q} \\ \boldsymbol{0} & \boldsymbol{0} & 0 \end{bmatrix} \begin{bmatrix} \delta\boldsymbol{q} \\ \delta\dot{\boldsymbol{q}} \\ Q \end{bmatrix} + \begin{bmatrix} \boldsymbol{0} & \boldsymbol{0} \\ 0 & 0 \\ \frac{\partial\ddot{\boldsymbol{r}}_N}{\partial Q_g} & \frac{\partial\ddot{\boldsymbol{r}}_N}{\partial T} \\ 1 & 0 \end{bmatrix} \begin{bmatrix} Q_g \\ T \end{bmatrix} + \boldsymbol{w}_y \tag{15}$$

[1] In general, the Kalman filter system vectors are different from the ones used for the linearization presented in Section 3.3, therefore the subscript KF (for Kalman Filter) is added to these vectors.

where $\ddot{\boldsymbol{r}}_N$ is the vector of nacelle accelerations, and $\tilde{\boldsymbol{q}} = \{\delta x, \delta y, \delta\phi_x, \delta\phi_y\}$ is the measurements of surge, sway, roll, and pitch as given in Table 1.

The state and output equations are used as part of a Kalman filter algorithm implemented in WELIB, which continuously takes as input the measurements from the wind turbine (corresponding to the left-hand side of Equation 15). The process and covariance matrices used within the Kalman filter algorithm (determining the values of $\boldsymbol{w}_x$ and $\boldsymbol{w}_y$) are populated based on the estimated standard deviations of the different states and outputs. At each time step, the thrust is estimated using the aerodynamic torque of the previous time step and used as input. The result of the Kalman filter ~~consists in~~ is the estimated states and outputs at each time step. Sample simulation results ~~will be~~ are provided in Section 4.

3.6 Virtual sensing

Once the states are estimated by the Kalman filter, the virtual sensing step is used to derive quantities of interest (see Figure 1). In this work, we focus on the estimation of the sectional loads along the tower using a physics-based model. We investigate two methods to obtain these loads.

3.6.1 OpenFAST linearization outputs

The first method consists of using the linearization outputs of OpenFAST, namely, using a subset of the equation $\delta\boldsymbol{y} = \boldsymbol{C}\delta\boldsymbol{x} + \boldsymbol{D}\delta\boldsymbol{u}$ (see Section 3.3.1). In general, if a ~~QoI~~ quantity of interest is present in the output vector of OpenFAST, it can be retrieved as follows. If the variable is located at the row index k in the vector $\boldsymbol{y}$, then this variable can be obtained from the states and inputs as:

$$[\boldsymbol{y}]_k = [\delta\boldsymbol{y}]_k + [\boldsymbol{y}_0]_k = [\boldsymbol{C}]_k\delta\boldsymbol{x} + [\boldsymbol{D}]_k\delta\boldsymbol{u} + [\boldsymbol{y}_0]_k \tag{16}$$

where $[\cdot]_k$ indicates that the row k of the matrix or column vector is used. In our case, $[\boldsymbol{y}]_k$ in Equation 16 would ~~for instance~~ be the sectional fore-aft bending moment at the height z_j along the tower, noted $\mathcal{M}_y(z_j)$. The advantages of using this method are multiple: 1) the method is directly applicable to any other outputs computed by OpenFAST, 2) the calculation procedure is linear and therefore computationally efficient, 3) if strain measurements are available at given heights, the rows $[\boldsymbol{C}]_k$ and $[\boldsymbol{D}]_k$ could be included in the output equation of the Kalman filter (Equation 15) to provide information about the model's expectation of these measurements, and 4) the underlying linear model is consistent with the nonlinear model of OpenFAST. The downside of the method is its linearity, in the sense that it is only valid close to the operating point and could lack important nonlinear effects. The values of $[\boldsymbol{C}]_k$, $[\boldsymbol{D}]_k$, and $[\boldsymbol{y}_0]_k$ would potentially need to be reevaluated if the system operates away from the linearized operating point. One possible solution ~~would be~~ is to introduce gain-scheduling to continuously modify the linear system based on the estimated wind speed. In this work, we used one operating point only and obtained results with fair accuracy (see Section 4). We nevertheless expect that to better represent the different operating regions of a pitch-regulated wind turbine, three to five linear models, stitched together through gain-scheduling would be needed.

3.6.2 Nonlinear calculation (WELIB)

An alternative method consists of computing the section loads based on first principles using the formulation presented in Branlard (2019). The calculation requires a knowledge of the tower-top loads and the full kinematics of the tower and nacelle (position, velocity, and acceleration). At a given time step, the kinematics are computed based on $\boldsymbol{q}$, $\dot{\boldsymbol{q}}$, and $\ddot{\boldsymbol{q}}$. The tower-top loads are estimated based on the aerodynamic loads and the inertial loads of the rotor-nacelle assembly. We describe the method in more ~~details~~ detail in Appendix D. The advantages are that nonlinearities are accounted for and the model is valid ~~irrespectively~~ irrespective of the operating condition. The downside is that this method does not provide any of the four advantages offered by the OpenFAST linearization method.

3.6.3 Verification of the section loads calculation

To verify the calculation of the section loads, we use the same “turbulent step” wind field and irregular sea state that ~~was~~ were used in Section 3.4.4. We assume that the time series of $\boldsymbol{q}$, $\dot{\boldsymbol{q}}$ and $\ddot{\boldsymbol{q}}$ are entirely known, extracted from the OpenFAST simulation. These time series are provided to the two section loads algorithms: the WELIB nonlinear algorithm ~~,~~ and the OpenFAST linear algorithm.

We run two sets of virtual sensing. In the “ideal” set, the loads at the tower top are extracted from OpenFAST results and provided to the two virtual sensing algorithms. In this ideal case, the linearized operating points of the OpenFAST linear model is set as the mean of each of the OpenFAST time series values. Results for the ideal case are ~~provided~~ illustrated in Figure 7. The two algorithms are able to reproduce the section loads of OpenFAST with relatively high accuracy, which verifies our two calculation procedures.

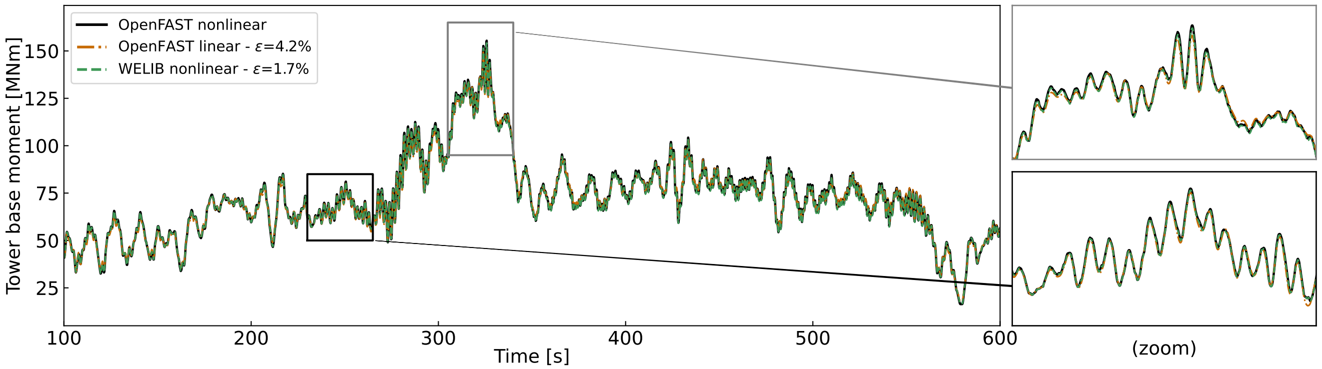

Figure 7. Tower fore-aft bending moment for the “turbulent step” and an irregular sea state as calculated by OpenFAST and compared to the WELIB nonlinear and OpenFAST linear method. The motion of the structure is determined by OpenFAST and provided to the two algorithms. The tower-top loads are also provided to the algorithms (“ideal” case, as opposed to Figure 8).

In the second set, labeled “unknown thrust~~”,~~,” the tower top loads are not provided to the algorithms~~, but~~; instead, the aerodynamic estimator mentioned in Section 3.4.4 is used to estimate the aerodynamic loads. This time, we do not set the linearized operating point of the OpenFAST linear model to the mean value of the time series~~, but~~; we set it to the static equilibrium (without loading).

The results are ~~provided~~ illustrated in Figure 8. The accuracy of the section loads calculation is seen to deteriorate when the aerodynamic loads are estimated with the aerodynamic estimator, which is expected. The damage equivalent load computed with a Wöhler slope of $m = 5$ is found to be 3.7% lower with the OpenFAST linear method and 1.2% lower with the YAMS nonlinear method compared to the value for reference signal.

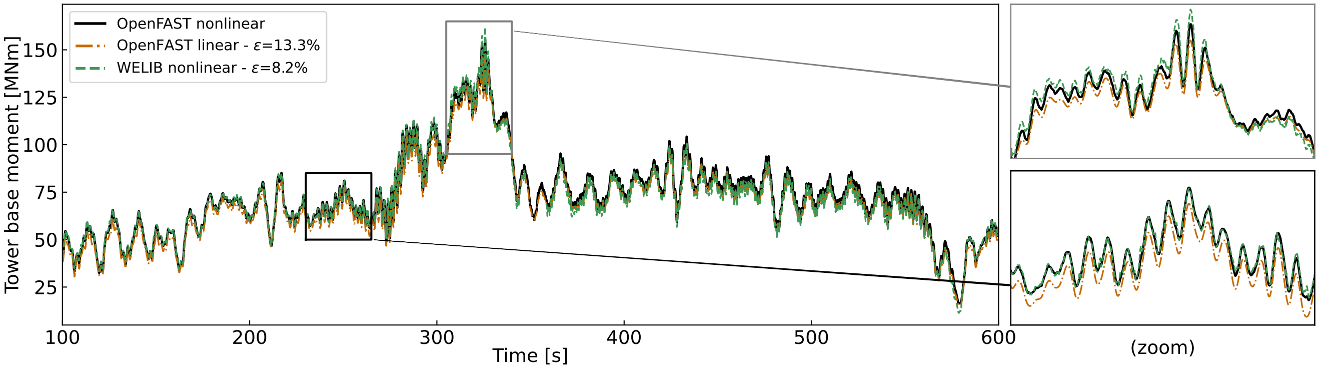

Figure 8. Tower fore-aft bending moment for the "turbulent step" and an irregular sea state as calculated by OpenFAST and compared to the WELIB nonlinear and the OpenFAST linear method. The motion of the structure is determined by OpenFAST and provided to the two other algorithms. The tower-top loads are estimated using the aerodynamic estimator ("unknown thrust" case, as opposed to the ideal case presented in Figure 7).

The ~~performances~~ performance of both algorithms ~~remain satisfactory because we observe that~~ remains satisfactory because the extrapolated signals follow the reference OpenFAST nonlinear simulation. The relative error obtained with the OpenFAST linear algorithm is higher (13.3%) than the one obtained using the WELIB nonlinear method (8.2%). The main source of error in the linear model is associated with the fact that the linearization point was not tuned for this specific simulation. It is our simplifying design choice to use only one linearization operating point throughout. Because of the loss of accuracy associated with this design choice, we ~~will~~ use the WELIB nonlinear algorithm in the digital twin for the calculation of section loads.

~~We note that the variable that affects the most~~ After performing a sensitivity analysis on the inputs and states of the system, we observed that the variables that most affect the fore-aft section loads ~~is~~ are the platform pitch (ϕ_y), the tower fore-aft bending degree of freedom (q_t), and ~~then,~~ the aerodynamic thrust. In this section, we assumed that all the states where known (including ϕ_y and q_t), leading to great accuracy in the estimation of the section loads. The final verification step ~~consists of~~ involves providing estimated states to the algorithm, which is the topic of the next section.

4 Applications of the digital twin

In Section 3 ~~,~~ we discussed how the different components of the digital twin were introduced and tested using increasing ~~level of~~ complexity. In this section, we ~~combine~~ discuss combining the different components to form the digital twin. We begin using numerical experiments from OpenFAST (see Section 2.3.2), similar to what was done ~~in the previous section~~previously, before using measurements from the TetraSpar prototype.

4.1 Numerical experiment

First, we use the same "turbulent step" wind field and sea state that was used throughout Section 3. The augmented states of the system are determined at each time step using the state estimator described in Section 3.5. The measurements (see Table 1) are taken from the nonlinear OpenFAST simulation. The wind speed and aerodynamic loads are estimated using the aerodynamic estimator described in Section 3.4. The linear model is derived from linearized OpenFAST~~while~~ , and the section loads in the tower are obtained using the WELIB virtual sensing algorithm described in Section 3.6. The estimates from the digital twin are compared with the reference nonlinear OpenFAST simulation results in Figure 9. A visual inspection of the time series reveals that the digital twin is able to capture the main trends and fluctuations of the different signals. The match can be considered remarkable given that only the sensors provided in Table 1 are used by the digital twin. Metrics such as mean relative error (ϵ) ~~,~~ and coefficient of determination (R^2) are indicated on the figure. Despite the visually appealing match, the metrics indicate that the tower-bottom moment has a mean error of $\epsilon = 21\%$. The damage equivalent load of the tower-bottom moment is

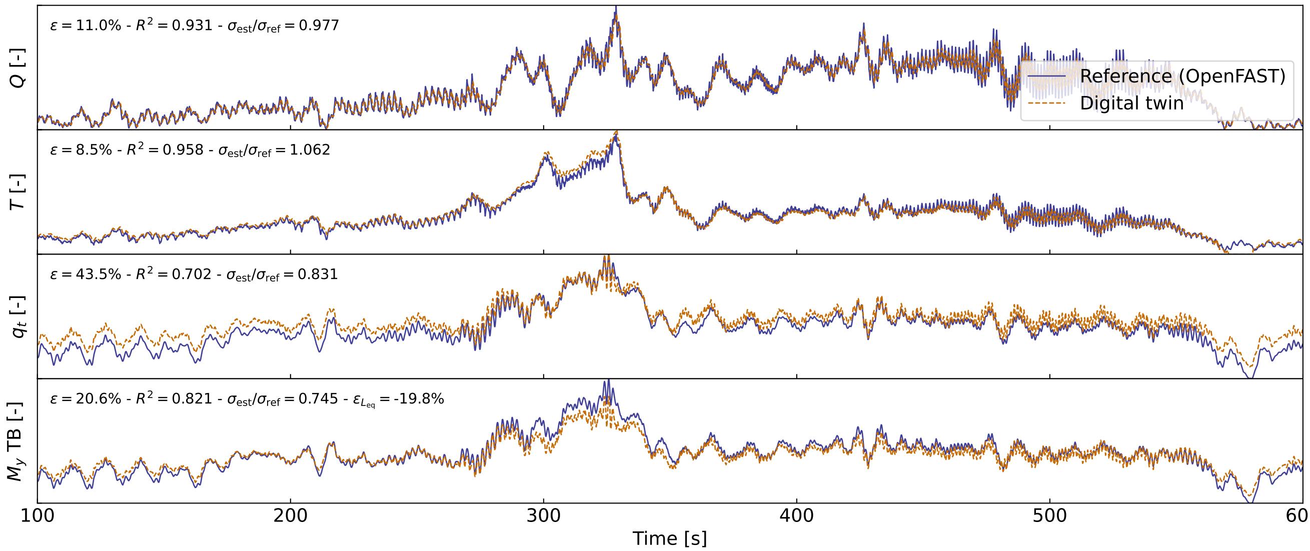

Figure 9. Estimated signals from the digital twin compared to results from ~~an~~ a nonlinear OpenFAST simulation using the turbulent-step numerical experiment. From top to bottom: aerodynamic torque (Q), aerodynamic thrust (T), tower-top position (q_t), tower-bottom fore-aft bending moment (M_y, TB). Results are made dimensionless for confidentiality reasons.

underestimated by $\tilde{\epsilon}_{L_{eq}} = -21\%$, where we define:

$$\tilde{\epsilon}(L_{eq}) = \frac{L_{eq,\mathrm{est}} - L_{eq,\mathrm{ref}}}{L_{eq,\mathrm{ref}}} \tag{17}$$

Differences in damage equivalent loads typically indicate differences in the frequency content of the signals. We compare the frequency content of the estimated signals with the reference signals in Figure 10. The low-frequency content (below 1 Hz) is captured well, in line with the visual inspection of Figure 9. Unfortunately, no clear trend is found for the ~~high frequency~~ high-frequency content: the power spectra of the aerodynamic loads indicate an underestimation, whereas the spectra of the tower-top position and tower-bottom bending moment tend to have higher energy content. As shown in previous studies (Branlard et al., 2020a), ~~adequate~~ filtering of the input measurements can be used to tune the energy content at high frequencies. The method is yet unsatisfactory because it acts as an artificial rebalancing of energy content to achieve the desired DEL value. Both low and high frequency content contribute to the DEL values, therefore, we believe that systematic improvement is only possible through modeling improvements and higher observability of the states by the Kalman filter.

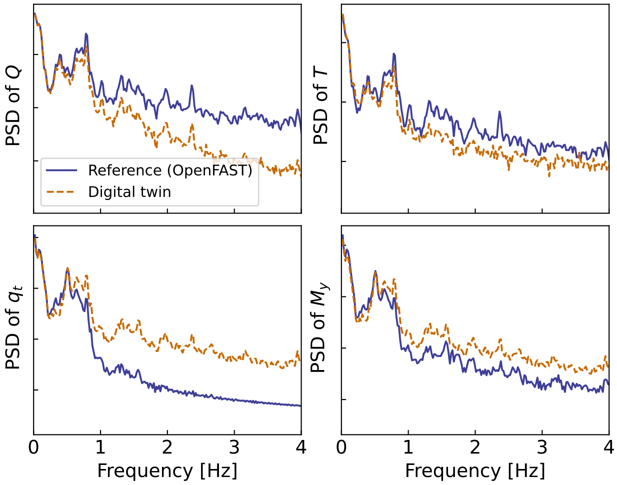

Figure 10. Power spectral density (PSD) of the time series presented in Figure 9. A logarithmic scale is used on the y axis.

To quantify the errors in the estimation under a wider set of operating conditions, we ~~ran~~ run 10-min simulations for a set of wind speeds under normal turbulent conditions and sea states. We ~~selected~~ select wind speeds from 5 to 20 m/s using 10 different seeds per bin of wind speed. The seeds are used to ~~randomise~~ randomize the turbulent field and sea states. The wind speed range is selected ~~such~~ so as to avoid cut-in and cut-out events where the aerodynamic estimator is not expected to perform well. The turbulence intensity is selected based on the normal turbulence model for a turbine of class “A~~”.~~.” The wave height and wave period are set as a function of the wind speed as: $H_s(U) = 0.16U + 1$ and ~~$T_p = 0.09U + 5.57$, based~~ $T_p(U) = 0.09U + 5.57$. The H_s and T_p relationships were obtained by performing a linear regression on the sea state and wind measurements at the test site. OpenFAST simulations ~~were~~ are run for each case, and then the digital twin ~~was~~ is run using these numerical measurements. A summary of the mean relative error on some key estimated quantities is given in Figure 11.

We observe that the mean relative error of the wind speed and aerodynamic loads ~~are~~ is between 5% and 15% with a tendency

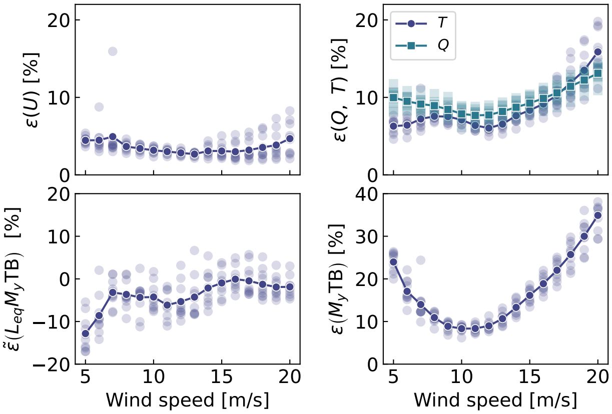

Figure 11. Mean relative error of estimated signals for various wind speed and seeds. Clockwise from top left: wind speed (U), aerodynamic loads, tower-bottom moment (M_y TB), and damage equivalent load of the tower-bottom moment (L_{eq,M_y} TB). The individual simulations are indicated by transparent markers. The average over each seed is indicated using ~~plain~~ solid lines.

for larger errors on the aerodynamic loads at low and high wind speeds. The error further propagates within the system, and the tower-bottom moment is estimated with a relative error between 10% and 40%. The error levels indicate that the aerodynamic estimator, which is based on quasi-steady rotor-averaged aerodynamics, cannot fully capture the dynamic aerodynamic state of the rotor in floating conditions. In general, the digital twin lacks sufficient information to fully capture the tower-top loads and the frequency content of the system. It is expected that ~~placing~~ the placement of additional sensors, such as accelerometers or load cells, along the tower ~~,~~ can significantly improve the estimation of the tower loads (in that case, we would either use OpenFAST linearization outputs ~~, or ,~~ or an extended Kalman filter and a nonlinear model for the outputs). As seen in Figure 11, the relative error levels on the damage equivalent loads are between -10% and 5%, with the loads being either overestimated or underestimated depending on the wind speed. The structural health monitoring system could potentially use the estimated error levels indicated in Figure 11 to provide a confidence interval on the fatigue lifetime of the tower. We note that these error levels represent a ~~best case scenario ,~~ best-case scenario because we assumed that no noise or biases were present in the measurements. We expect the error levels to increase with additional measurement noise.

4.2 Estimations using measurements from the full-scale prototype

In this section, we use measurements from the full-scale TetraSpar prototype installed off the Norwegian coast. Four days of data were selected based on data availability; a wide range of wind speeds are present in the time series (ranging from 4 to 24.5 $\mathrm{m/s}$ with an overall mean of 8.9 m/s). Two days were selected in summer and two in winter to account for potential seasonality. Apart from these criteria, the selection of time series can be considered random. The measurement data ~~is~~ are stored as 10-min time series sampled at 25 Hz. The total number of 10-min samples used over the four days is 576. The measurement data ~~is~~

are provided to the digital twin to perform the state estimation and virtual sensing. ~~The~~ The prototype is equipped with load cells at the tower top, middle, and bottom and nacelle wind speed measurements. We use these measurements to compare with the digital twin estimates.

We begin by highlighting the computational time of the current procedure, as computational efficiency is crucial to achieve our digital twin vision. The state estimation is currently 10 times faster than ~~realtime~~real time. The virtual sensing step is ~~half realtime~~ twice as fast as real time, but computational improvements are possible, in particular, by using a compiled language instead of Python. ~~The prototype is equipped with load cells at the tower top, middle and bottom, and nacelle wind speed measurements. We use these measurements to compare with~~ For reference, OpenFAST simulations of the full TetraSpar model (with substructure flexibility) typically run 3 times slower than real time, and a reduced-order OpenFAST model with 8 DOF runs 1.1 times slower. Currently, real time estimation cannot be achieved with OpenFAST. Reduced-order modeling techniques, such as the ones presented in this article, are necessary to implement an online digital twin. Yet, if the digital twin ~~estimates.~~is run as a postprocessing step, then parallelization using multiple CPUs could be used, e.g., processing different time periods of the day.

A sample of results is provided in Figure 12. The figure illustrates a selected case where the estimation of the tower load is reasonably accurate, with an error on the damage equivalent load of only 0.4%. We note that the wind speed from the measurement is a point measurement ~~,~~ (nacelle anenometer, in the wake of the turbine), and it is therefore not expected to be in strong agreement with the digital twin estimate, which is representative of a rotor-averaged wind speed.

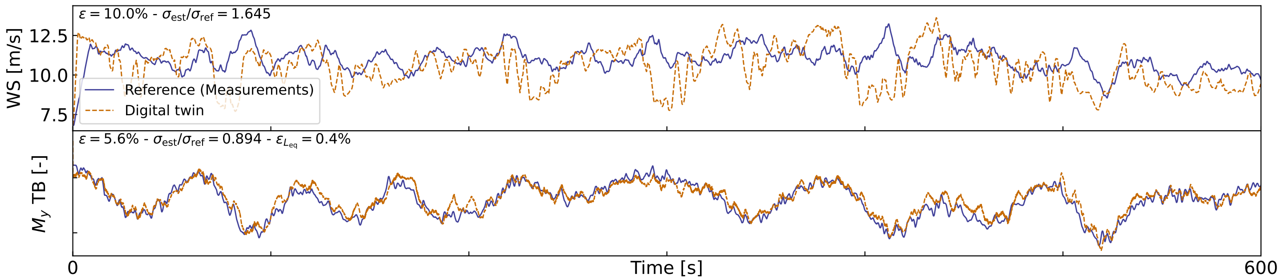

Figure 12. Comparison of digital twin outputs with wind speed and tower-bottom moment measurements from the TetraSpar prototype. The measured wind speed comes from a nacelle anenometer and therefore is expected to differ from the rotor-averaged value estimated by the digital twin.

An aggregate of results from all the 10-min digital twin runs is illustrated in Figure 13. The figure shows relative errors in wind speed, thrust, and damage equivalent loads at the tower bottom and tower middle. As indicated previously, the wind speed from the digital twin and the measurements are different quantities, but the level of error obtained indicates that the digital twin is able to capture the main level of wind speed. The aerodynamic thrust from the aerodynamic estimator is compared with the load cell at the tower top in the fore-aft direction. This is a crude first-order approximation ~~,~~ (e.g., neglecting inertial and gravitational loads, nacelle tilting and shaft bending), but the overall estimated levels appears to be~~on average~~, on average, around 10% from the measured ones. The tower damage equivalent loads are~~on average~~, on average, within ±10% of the

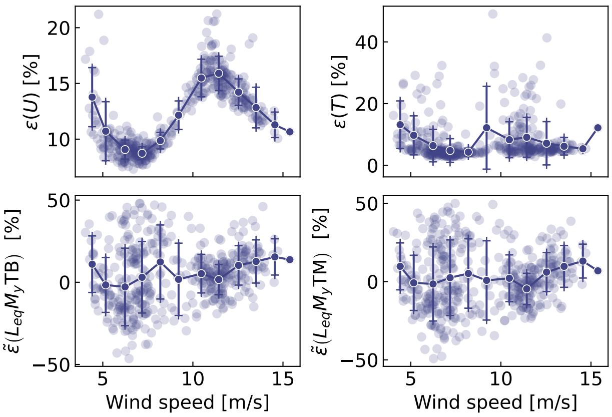

Figure 13. Similar to Figure 11 but using measurements from the Tetra Spar prototype. Each marker ~~indicate~~ indicates a ~~10~~ 10-min simulation result. Solid lines are bin averages. The whiskers indicate the standard deviation in each bin. The bottom plots are for the tower bottom (TB) and tower middle (TM) bending moments.

values obtained from the measurements, but some cases show errors ranging between ±50%. To give perspective on the large error values taken by the metrics, we illustrate two cases with large errors in Figure 14 and Figure 15. In both cases, we observe

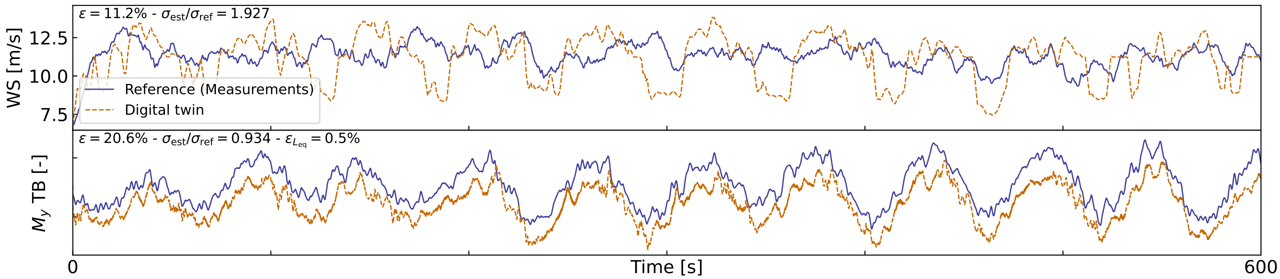

Figure 14. Similar to Figure 12, but for a case where a clear offset is present in the tower loads.

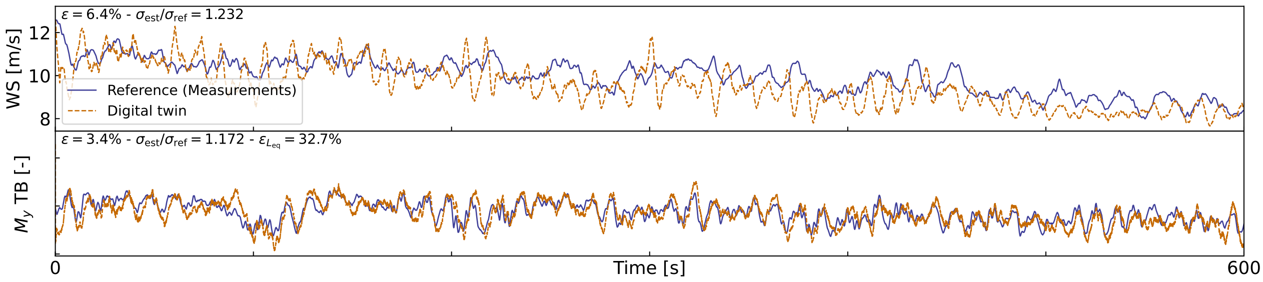

Figure 15. Similar to Figure 12, but for a case where a large error in damage equivalent load is observed.

that the estimator is capturing the trends and low frequencies with ~~accuracies~~ accuracy that, from a pure qualitative perspective, would appear satisfactory. As seen in Figure 14, an offset is present in the signal, which indicates that some physics might be missing from the load virtual sensing, or that the state estimator is failing. Measurement errors could also affect the results, but no systematic error was detected over the time period investigated. It is therefore difficult to conclude as to what is the main source of error. In Figure 14, the overall load level is captured well, but the error in the damage equivalent load is $\epsilon_{L_{eq}}$ is 33%. As illustrated in Figure 10, our current method fails at capturing the high-frequency content of the signals, which can have a significant impact on the accuracy of the damage equivalent loads. ~~In spite of~~ Despite these challenges, the average accuracy of 10% is promising and indicates that the current methodology can be used to reconstruct some structural and environmental signals from a limited number of ~~readily-available~~ readily available sensors.

5 Conclusions

In this work, we implemented, verified, and validated a physics-based digital twin solution applied to a floating offshore wind turbine. The work focused on the estimation of the aerodynamic loads and the section loads along the tower, using a set of measurements that we expect to be available on any existing wind turbine (power, pitch, rotor speed, and tower acceleration) ~~,~~ and motion sensors that are likely to be standard measurements for a floating platform (inclination and GPS sensors). The key concept behind our approach ~~consists of using:~~ uses 1) a Kalman filter to estimate the structural states based on a linear model of the structure and measurements from the turbine, 2) an aerodynamic estimator, and 3) a physics-based virtual sensing procedure to obtain the loads along the tower. An important part of the work ~~consisted of~~ was developing the methodology and implementing the tools and models necessary for the aerodynamic estimation, state estimation, and load virtual sensing. We explored two different pathways to obtain models: a suite of Python tools ~~, or~~ and OpenFAST linearization. We used components from both approaches for the digital twin.

Using numerical experiments, we found that the accuracy of the individual models ~~were typically in~~ was typically on the order of 5%. When comparing the digital twin estimations with the measurements from the TetraSpar prototype, the errors increased to 10%~~-~~–15% on average for the quantities of interest. Overall, the accuracy of the results appeared promising given the scope of our work, which aimed ~~at illustrating~~ to illustrate a proof of concept for a floating wind turbine digital twin. We observed a non-negligible scatter of results for the estimation of the tower damage equivalent loads that we attributed to the difficulty of capturing high-frequency content.

Future work ~~,~~ should therefore explore possible improvements of the method to address this issue.

Additional improvements could include: 1) gain-scheduling of the linear models ~~,~~ to extend the domain of validity of the linear models used and reduce the modeling error, 2) using nonlinear models and extended Kalman filtering techniques ~~,~~ to lift the linear assumptions that challenges the aerodynamics, hydrodynamics and structural dynamics, 3) introducing additional degrees of freedom and a full account of the yawing of the nacelle ~~,~~ to increase the fidelity of the models and account for the flexibility of the floater, 4) adding a model to account for wave excitation forces ~~,~~ to account for hydrodynamic loads and likely improve the estimation of member-level loads, 5) introducing additional measurements ~~,~~ to improve the state estimation and increase the observability of the state, 6) improving the robustness of the aerodynamic estimator ~~(in particular~~in particular, beyond the cut-in and cut-out wind ~~speed), and~~ speeds, to apply the digital twin when the turbine is not operating, and, 7) expanding the virtual sensing steps to estimate additional signals.

Author contributions. EB implemented the digital twin and wrote the main corpus of this paper. JJ, CB and JZ provided continuous feedback on the project and reviewed the article.

Competing interests. No competing interests are present.

Code availability. The source code of the digital twin and examples using a generic spar turbine are provided in the GitHub repository (Branlard, 2023a).

Acknowledgements. This work was authored in part by the National Renewable Energy Laboratory, operated by Alliance for Sustainable Energy, LLC, for the U.S. Department of Energy (DOE) under Contract No. DE-AC36-08GO28308. Funding provided by U.S. Department of Energy Office of Energy Efficiency and Renewable Energy Wind Energy Technologies Office. The views expressed in the article do not necessarily represent the views of the DOE or the U.S. Government. The U.S. Government retains and the publisher, by accepting the article for publication, acknowledges that the U.S. Government retains a nonexclusive, paid-up, irrevocable, worldwide license to publish or reproduce the published form of this work, or allow others to do so, for U.S. Government purposes.

Financial support. This work was funded under the Technology Commercialization Fund Project, supported by DOE's Wind Energy Technologies Office.

Appendix A: Linearization of the equations of motion with augmented inputs

In this section, we describe the procedure used to linearize the structural equations of motion without ~~a~~ knowledge of the external loads, which is used to obtain Equation 1. We write the implicit form of the equations of motion as

$$\mathbf{e}(\boldsymbol{q}, \dot{\boldsymbol{q}}, \ddot{\boldsymbol{q}}, \tilde{\boldsymbol{u}}, t) = \mathbf{0} \tag{A1}$$

where $\boldsymbol{q}$, $\dot{\boldsymbol{q}}$, $\ddot{\boldsymbol{q}}$ and $\tilde{\boldsymbol{u}}$ are the degrees of freedom, velocities, accelerations, and "augmented inputs" of the model, respectively. The term augmented input is used because the external loads are included in this vector. The external loads are (in general) a function of the degrees of freedom. Therefore, we write the augmented input vector as:

$$\tilde{\boldsymbol{u}} = \tilde{\boldsymbol{u}}(\boldsymbol{q}, \dot{\boldsymbol{q}}, \ddot{\boldsymbol{q}}, \boldsymbol{u}) \tag{A2}$$

where $\boldsymbol{u}$ is the vector of inputs in the classical sense, that is, consisting of system inputs that do not depend on the degrees of freedom (for instance, the wave elevation). The operating point is written using the subscript “0~~”,and~~,” and is defined as:

$$\mathbf{e}(\boldsymbol{q}_0, \dot{\boldsymbol{q}}_0, \ddot{\boldsymbol{q}}_0, \tilde{\boldsymbol{u}}_0, t) = \mathbf{0} \tag{A3}$$

We perturb each variable, as $\boldsymbol{q} = \boldsymbol{q}_0 + \delta\boldsymbol{q}$, $\dot{\boldsymbol{q}} = \dot{\boldsymbol{q}}_0 + \delta\dot{\boldsymbol{q}}$, etc., where δ indicates a small perturbation of the quantities. The perturbation of the augmented input is then:

$$\tilde{\boldsymbol{u}} = \tilde{\boldsymbol{u}}(\boldsymbol{q}_0, \dot{\boldsymbol{q}}_0, \ddot{\boldsymbol{q}}_0, \boldsymbol{u}_0) + \left.\frac{\partial \tilde{\boldsymbol{u}}}{\partial \boldsymbol{q}}\right|_0 \delta\boldsymbol{q} + \left.\frac{\partial \tilde{\boldsymbol{u}}}{\partial \dot{\boldsymbol{q}}}\right|_0 \delta\dot{\boldsymbol{q}} + \left.\frac{\partial \tilde{\boldsymbol{u}}}{\partial \ddot{\boldsymbol{q}}}\right|_0 \delta\ddot{\boldsymbol{q}} + \left.\frac{\partial \tilde{\boldsymbol{u}}}{\partial \boldsymbol{u}}\right|_0 \delta\boldsymbol{u} \tag{A4}$$

where $|_0$ indicates that the expressions are evaluated at the operating point. The linearized equations are obtained using a ~~Taylor-Series~~ Taylor-series expansion:

$$\left[\boldsymbol{M}_0 - \boldsymbol{Q}_0 \left.\frac{\partial \tilde{\boldsymbol{u}}}{\partial \ddot{\boldsymbol{q}}}\right|_0\right] \boldsymbol{\delta}\ddot{\boldsymbol{q}} + \left[\boldsymbol{C}_0 - \boldsymbol{Q}_0 \left.\frac{\partial \tilde{\boldsymbol{u}}}{\partial \dot{\boldsymbol{q}}}\right|_0\right] \boldsymbol{\delta}\dot{\boldsymbol{q}} + \left[\boldsymbol{K}_0 - \boldsymbol{Q}_0 \left.\frac{\partial \tilde{\boldsymbol{u}}}{\partial \boldsymbol{q}}\right|_0\right] \boldsymbol{\delta q} = \boldsymbol{Q}_0 \left.\frac{\partial \tilde{\boldsymbol{u}}}{\partial \boldsymbol{u}}\right|_0 \boldsymbol{\delta u} \tag{A5}$$

with

$$\boldsymbol{M}_0 = -\left.\frac{\partial \mathbf{e}}{\partial \ddot{\boldsymbol{q}}}\right|_0, \quad \boldsymbol{C}_0 = -\left.\frac{\partial \mathbf{e}}{\partial \dot{\boldsymbol{q}}}\right|_0, \quad \boldsymbol{K}_0 = -\left.\frac{\partial \mathbf{e}}{\partial \boldsymbol{q}}\right|_0, \quad \boldsymbol{Q}_0 = \left.\frac{\partial \mathbf{e}}{\partial \boldsymbol{u}}\right|_0 \tag{A6}$$

and where $\boldsymbol{M}_0$, $\boldsymbol{C}_0$, $\boldsymbol{K}_0$ are the linear mass, damping, and stiffness matrices, and $\boldsymbol{Q}_0$ is the linear forcing vector, also called the input matrix.

Appendix B: Transfer of a Jacobian from one destination point to another

The Jacobians provided by OpenFAST and MAP are provided at given nodes of the structure (e.g., the hydrodynamic nodes, or the fairleads). In this section, we highlight the procedure to transfer these Jacobians to another node (the platform reference point) assuming a rigid-body relationship between the nodes. The procedure is used in this work to compute the linear 6 × 6 matrix for the hydrodynamics and mooring dynamics in Section 3.3.2. We obtain different relationships depending ~~if~~ on whether the destination point is assumed to be displaced or not ~~.~~(see different subsections below).

B1 Transfer of Jacobians between two points

We consider a point source (noted S) and a destination point (noted D). The notations are illustrated in Figure B1. We assume ~~a rigid-body~~

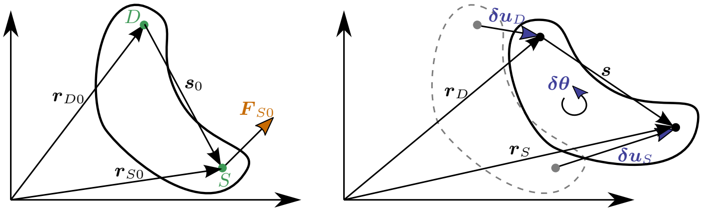

Figure B1. Rigid-body kinematics with the loads from one source point (S) transferred to ta destination point (D), assuming small motion of the points.

~~relationship between~~ that the two points ~~.~~ belong to a rigid body. The forces and moments at the destination and source are related as follows:

$$\boldsymbol{F}_D = \boldsymbol{F}_S \tag{B1}$$

$$\boldsymbol{M}_D = \boldsymbol{M}_S + \tilde{\boldsymbol{s}}\boldsymbol{F}_S \tag{B2}$$

where $\boldsymbol{s} = \boldsymbol{r}_S - \boldsymbol{r}_D$ is the vector from destination point to the source point, $\boldsymbol{F}_S$ and $\boldsymbol{M}_S$ are the force and moments, respectively, at point S, and the tilde notation refers to the skew symmetric matrix, which is a matrix representation of the cross product. We seek to linearize Equation B1 and Equation B2 for small displacements and rotations of the destination and source nodes. In particular, we seek to express the Jacobians at the destination node as a function of the source node, assuming a rigid-body relationship between the two. The rigid-body relationship linking the small displacements ($\delta\boldsymbol{u}$) and small rotations ($\delta\boldsymbol{\theta}$) of the source and destination points is:

$$\begin{aligned} \delta\boldsymbol{u}_D &= \delta\boldsymbol{u}_S + \tilde{\boldsymbol{s}}_\mathbf{0}\delta\boldsymbol{\theta}_S \\ \delta\boldsymbol{\theta}_D &= \delta\boldsymbol{\theta}_S \end{aligned} \tag{B3}$$

where $\boldsymbol{s}_0$ is the vector between the source and destination points at the operating point (prior to the perturbation). The Jacobians of the transformations given in Equation B3~~(~~, and its inverse~~)~~, are:

$$\begin{bmatrix} \frac{\partial \boldsymbol{u}_D}{\partial \boldsymbol{u}_S} & \frac{\partial \boldsymbol{u}_D}{\partial \boldsymbol{\theta}_S} \\ \frac{\partial \boldsymbol{\theta}_D}{\partial \boldsymbol{u}_S} & \frac{\partial \boldsymbol{\theta}_D}{\partial \boldsymbol{\theta}_S} \end{bmatrix} = \begin{bmatrix} \boldsymbol{I} & \tilde{\boldsymbol{s}}_\mathbf{0} \\ \mathbf{0} & \boldsymbol{I} \end{bmatrix}, \qquad \begin{bmatrix} \frac{\partial \boldsymbol{u}_S}{\partial \boldsymbol{u}_D} & \frac{\partial \boldsymbol{u}_S}{\partial \boldsymbol{\theta}_D} \\ \frac{\partial \boldsymbol{\theta}_S}{\partial \boldsymbol{u}_D} & \frac{\partial \boldsymbol{\theta}_S}{\partial \boldsymbol{\theta}_D} \end{bmatrix} = \begin{bmatrix} \boldsymbol{I} & -\tilde{\boldsymbol{s}}_\mathbf{0} \\ \mathbf{0} & \boldsymbol{I} \end{bmatrix} \tag{B4}$$

To linearize Equation B1 and Equation B2, we introduce the following perturbations:

$$\boldsymbol{F}_D = \boldsymbol{F}_{D0} + \delta\boldsymbol{F}_D, \quad \boldsymbol{F}_S = \boldsymbol{F}_{S0} + \delta\boldsymbol{F}_S \tag{B5}$$

$$\boldsymbol{M}_D = \boldsymbol{M}_{D0} + \delta\boldsymbol{M}_D, \quad \boldsymbol{M}_S = \boldsymbol{M}_{S0} + \delta\boldsymbol{M}_S, \tag{B6}$$

where the subscript 0 indicates values at the operating point. At the operating point, Equation B1 and Equation B2 are satisfied, that is:

$$\boldsymbol{F}_{D0} = \boldsymbol{F}_{S0} \tag{B7}$$

$$\boldsymbol{M}_{D0} = \boldsymbol{M}_{S0} + \tilde{\boldsymbol{s}}_\mathbf{0}\boldsymbol{F}_{S0} \tag{B8}$$

Transfer of forces

Inserting Equation B5 into Equation B1 leads to:

$$\boldsymbol{F}_{D0} + \delta\boldsymbol{F}_D = \boldsymbol{F}_{S0} + \delta\boldsymbol{F}_S \tag{B9}$$

~~Which~~which, using Equation B7, leads to:

$$\delta\boldsymbol{F}_D = \delta\boldsymbol{F}_S \tag{B10}$$

The Jacobians of the loads at node D with respect to the displacements at node D are then obtained by applying the chain rule to Equation B10 and making use of the Jacobian of the displacements given on the right of Equation B4. For instance, for the force:

$$\begin{aligned} \frac{\partial \boldsymbol{F}_D}{\partial \boldsymbol{u}_D} &= \frac{\partial \boldsymbol{F}_S}{\partial \boldsymbol{u}_S}\frac{\partial \boldsymbol{u}_S}{\partial \boldsymbol{u}_D} + \frac{\partial \boldsymbol{F}_S}{\partial \boldsymbol{\theta}_S}\frac{\partial \boldsymbol{\theta}_S}{\partial \boldsymbol{u}_D} = \frac{\partial \boldsymbol{F}_S}{\partial \boldsymbol{u}_S} \\ \frac{\partial \boldsymbol{F}_D}{\partial \boldsymbol{\theta}_D} &= \frac{\partial \boldsymbol{F}_S}{\partial \boldsymbol{u}_S}\frac{\partial \boldsymbol{u}_S}{\partial \boldsymbol{\theta}_D} + \frac{\partial \boldsymbol{F}_S}{\partial \boldsymbol{\theta}_S}\frac{\partial \boldsymbol{\theta}_S}{\partial \boldsymbol{\theta}_D} = \frac{\partial \boldsymbol{F}_S}{\partial \boldsymbol{\theta}_S} - \frac{\partial \boldsymbol{F}_S}{\partial \boldsymbol{u}_S}\tilde{\boldsymbol{s}}_\mathbf{0} \end{aligned} \tag{B11}$$

For the transfer of the moments, the relationship will be different whether the moments are transferred at the undisplaced destination point ~~,~~ or the displaced destination point.

Moments at the undisplaced destination point

In this section, the moments are transferred to the undisplaced destination point. The vector from the undisplaced destination point to the displaced source is:

$$\boldsymbol{r} = \boldsymbol{s}_0 + \delta \boldsymbol{u}_S \tag{B12}$$

Introducing Equation B6 and Equation B12 into Equation B2, and temporarily using the "×" notation instead of the tilde notation:

$$\boldsymbol{M}_{D0} + \delta \boldsymbol{M}_D = \boldsymbol{M}_{S0} + \delta \boldsymbol{M}_S + \boldsymbol{s}_0 \times \boldsymbol{F}_{S0} + \boldsymbol{s}_0 \times \delta \boldsymbol{F}_S + \delta \boldsymbol{u}_S \times \boldsymbol{F}_{S0} + \delta \boldsymbol{u}_S \times \delta \boldsymbol{F}_S \tag{B13}$$

Making use of Equation B8, neglecting the nonlinear term ($\delta \boldsymbol{u}_S \times \delta \boldsymbol{F}_S$) and reintroducing the tilde notation ~~,~~leads to:

$$\delta \boldsymbol{M}_D = \delta \boldsymbol{M}_S + \tilde{\boldsymbol{s}}_{\boldsymbol{0}} \delta \boldsymbol{F}_S - \tilde{\boldsymbol{F}}_{S0} \delta \boldsymbol{u}_S \tag{B14}$$

The Jacobians of the moments at the undisplaced node D with respect to the displacements at node D are then obtained by applying the chain rule to Equation B14:

$$\begin{aligned}
\frac{\partial \boldsymbol{M}_D}{\partial \boldsymbol{u}_D} &= \frac{\partial \boldsymbol{M}_S}{\partial \boldsymbol{u}_S}\frac{\partial \boldsymbol{u}_S}{\partial \boldsymbol{u}_D} + \frac{\partial \boldsymbol{M}_S}{\partial \boldsymbol{\theta}_S}\frac{\partial \boldsymbol{\theta}_S}{\partial \boldsymbol{u}_D} + \tilde{\boldsymbol{s}}_{\boldsymbol{0}}\left[\frac{\partial \boldsymbol{F}_S}{\partial \boldsymbol{u}_S}\frac{\partial \boldsymbol{u}_S}{\partial \boldsymbol{u}_D} + \frac{\partial \boldsymbol{F}_S}{\partial \boldsymbol{\theta}_S}\frac{\partial \boldsymbol{\theta}_S}{\partial \boldsymbol{u}_D}\right] - \tilde{\boldsymbol{F}}_{S0}\frac{\partial \boldsymbol{u}_S}{\partial \boldsymbol{u}_D} \\
&= \frac{\partial \boldsymbol{M}_S}{\partial \boldsymbol{u}_S} + \tilde{\boldsymbol{s}}_{\boldsymbol{0}}\frac{\partial \boldsymbol{F}_S}{\partial \boldsymbol{u}_S} - \tilde{\boldsymbol{F}}_{S0}
\end{aligned} \tag{B15}$$

and

$$\begin{aligned}
\frac{\partial \boldsymbol{M}_D}{\partial \boldsymbol{\theta}_D} &= \frac{\partial \boldsymbol{M}_S}{\partial \boldsymbol{\theta}_S}\frac{\partial \boldsymbol{\theta}_S}{\partial \boldsymbol{\theta}_D} + \frac{\partial \boldsymbol{M}_S}{\partial \boldsymbol{u}_S}\frac{\partial \boldsymbol{u}_S}{\partial \boldsymbol{\theta}_D} + \tilde{\boldsymbol{s}}_{\boldsymbol{0}}\left[\frac{\partial \boldsymbol{F}_S}{\partial \boldsymbol{\theta}_S}\frac{\partial \boldsymbol{\theta}_S}{\partial \boldsymbol{\theta}_D} + \frac{\partial \boldsymbol{F}_S}{\partial \boldsymbol{u}_S}\frac{\partial \boldsymbol{u}_S}{\partial \boldsymbol{\theta}_D}\right] - \tilde{\boldsymbol{F}}_{S0}\frac{\partial \boldsymbol{u}_S}{\partial \boldsymbol{\theta}_D} \\
&= \frac{\partial \boldsymbol{M}_S}{\partial \boldsymbol{\theta}_S} - \frac{\partial \boldsymbol{M}_S}{\partial \boldsymbol{u}_S}\tilde{\boldsymbol{s}}_{\boldsymbol{0}} + \tilde{\boldsymbol{s}}_{\boldsymbol{0}}\frac{\partial \boldsymbol{F}_S}{\partial \boldsymbol{\theta}_S} - \tilde{\boldsymbol{s}}_{\boldsymbol{0}}\frac{\partial \boldsymbol{F}_S}{\partial \boldsymbol{u}_S}\tilde{\boldsymbol{s}}_{\boldsymbol{0}} + \tilde{\boldsymbol{F}}_{S0}\tilde{\boldsymbol{s}}_{\boldsymbol{0}}
\end{aligned} \tag{B16}$$

Jacobian relationships at the undisplaced destination point

Equation B11, Equation B16, and Equation B15 can be gathered in matricial form to relate the different Jacobians between the source point and the undisplaced destination point:

$$\begin{bmatrix} \frac{\partial \boldsymbol{F}_D}{\partial \boldsymbol{u}_D} & \frac{\partial \boldsymbol{F}_D}{\partial \boldsymbol{\theta}_D} \\ \frac{\partial \boldsymbol{M}_D}{\partial \boldsymbol{u}_D} & \frac{\partial \boldsymbol{M}_D}{\partial \boldsymbol{\theta}_D} \end{bmatrix}_{\text{undisplaced}} = \begin{bmatrix} \boldsymbol{I} & \boldsymbol{0} \\ \tilde{\boldsymbol{s}}_{\boldsymbol{0}} & \boldsymbol{I} \end{bmatrix} \begin{bmatrix} \frac{\partial \boldsymbol{F}_S}{\partial \boldsymbol{u}_S} & \frac{\partial \boldsymbol{F}_S}{\partial \boldsymbol{\theta}_S} \\ \frac{\partial \boldsymbol{M}_S}{\partial \boldsymbol{u}_S} & \frac{\partial \boldsymbol{M}_S}{\partial \boldsymbol{\theta}_S} \end{bmatrix} \begin{bmatrix} \boldsymbol{I} & -\tilde{\boldsymbol{s}}_{\boldsymbol{0}} \\ \boldsymbol{0} & \boldsymbol{I} \end{bmatrix} + \begin{bmatrix} \boldsymbol{0} & \boldsymbol{0} \\ -\tilde{\boldsymbol{F}}_{S0} & \tilde{\boldsymbol{F}}_{S0}\tilde{\boldsymbol{s}}_{\boldsymbol{0}} \end{bmatrix} \tag{B17}$$

Moments at the displaced destination point

In this section, the moments are transferred to the displaced destination point. The vector from the displaced destination point to the displaced source is:

$$\boldsymbol{r} = \boldsymbol{s}_0 + \delta \boldsymbol{u}_S - \delta \boldsymbol{u}_D = \boldsymbol{s}_0 - \tilde{\boldsymbol{s}}_{\boldsymbol{0}} \delta \boldsymbol{\theta}_S \tag{B18}$$

Introducing Equation B6 and Equation B18 into Equation B2, and temporarily using the "×" notation instead of the tilde notation:

$$\boldsymbol{M}_{D0} + \delta \boldsymbol{M}_D = \boldsymbol{M}_{S0} + \delta \boldsymbol{M}_S + \boldsymbol{s}_0 \times \boldsymbol{F}_{S0} + \boldsymbol{s}_0 \times \delta \boldsymbol{F}_S - (\boldsymbol{s}_0 \times \delta \boldsymbol{\theta}_S) \times \boldsymbol{F}_{S0} - (\boldsymbol{s}_0 \times \delta \boldsymbol{\theta}_S) \times \delta \boldsymbol{F}_S \tag{B19}$$

Making use of Equation B8, neglecting the nonlinear term $((\boldsymbol{s}_0 \times \delta\boldsymbol{\theta}_S) \times \delta\boldsymbol{F}_S)$, and reintroducing the tilde notation ~~,~~ leads to:

$$\delta\boldsymbol{M}_D = \delta\boldsymbol{M}_S + \tilde{\boldsymbol{s}}_\mathbf{0}\delta\boldsymbol{F}_S + \tilde{\boldsymbol{F}}_{S0}\tilde{\boldsymbol{s}}_\mathbf{0}\delta\boldsymbol{\theta}_S \tag{B20}$$

The Jacobians of the loads at the displaced node D with respect to the displacements at node D are then obtained by applying the chain rule to Equation B20 and making use of the Jacobian of the displacements given on the right of Equation B4.

$$\begin{aligned}\frac{\partial\boldsymbol{M}_D}{\partial\boldsymbol{u}_D} &= \frac{\partial\boldsymbol{M}_S}{\partial\boldsymbol{u}_S}\frac{\partial\boldsymbol{u}_S}{\partial\boldsymbol{u}_D} + \frac{\partial\boldsymbol{M}_S}{\partial\boldsymbol{\theta}_S}\frac{\partial\boldsymbol{\theta}_S}{\partial\boldsymbol{u}_D} + \tilde{\boldsymbol{s}}_\mathbf{0}\frac{\partial\boldsymbol{F}_S}{\partial\boldsymbol{u}_S}\\ &= \frac{\partial\boldsymbol{M}_S}{\partial\boldsymbol{u}_S} + \tilde{\boldsymbol{s}}_\mathbf{0}\frac{\partial\boldsymbol{F}_S}{\partial\boldsymbol{u}_S}\end{aligned} \tag{B21}$$

and

$$\begin{aligned}\frac{\partial\boldsymbol{M}_D}{\partial\boldsymbol{\theta}_D} &= \frac{\partial\boldsymbol{M}_S}{\partial\boldsymbol{u}_S}\frac{\partial\boldsymbol{u}_S}{\partial\boldsymbol{\theta}_D} + \frac{\partial\boldsymbol{M}_S}{\partial\boldsymbol{\theta}_S}\frac{\partial\boldsymbol{\theta}_S}{\partial\boldsymbol{\theta}_D} + \tilde{\boldsymbol{s}}_\mathbf{0}\frac{\partial\boldsymbol{F}_S}{\partial\boldsymbol{\theta}_D} + \tilde{\boldsymbol{F}}_{S0}\tilde{\boldsymbol{s}}_\mathbf{0}\\ &= \frac{\partial\boldsymbol{M}_S}{\partial\boldsymbol{\theta}_S} - \frac{\partial\boldsymbol{M}_S}{\partial\boldsymbol{u}_S}\tilde{\boldsymbol{s}}_\mathbf{0} + \tilde{\boldsymbol{s}}_\mathbf{0}\frac{\partial\boldsymbol{F}_S}{\partial\boldsymbol{\theta}_D} + \tilde{\boldsymbol{F}}_{S0}\tilde{\boldsymbol{s}}_\mathbf{0}\\ &= \frac{\partial\boldsymbol{M}_S}{\partial\boldsymbol{\theta}_S} - \frac{\partial\boldsymbol{M}_S}{\partial\boldsymbol{u}_S}\tilde{\boldsymbol{s}}_\mathbf{0} + \tilde{\boldsymbol{s}}_\mathbf{0}\frac{\partial\boldsymbol{F}_S}{\partial\boldsymbol{\theta}_S} - \tilde{\boldsymbol{s}}_\mathbf{0}\frac{\partial\boldsymbol{F}_S}{\partial\boldsymbol{u}_S}\tilde{\boldsymbol{s}}_\mathbf{0} + \tilde{\boldsymbol{F}}_{S0}\tilde{\boldsymbol{s}}_\mathbf{0}\end{aligned} \tag{B22}$$

Jacobian relationships at the displaced destination point

Equation B11, Equation B22, and Equation B21 can be gathered in matricial form to relate the different Jacobians:

$$\begin{bmatrix}\frac{\partial\boldsymbol{F}_D}{\partial\boldsymbol{u}_D} & \frac{\partial\boldsymbol{F}_D}{\partial\boldsymbol{\theta}_D}\\ \frac{\partial\boldsymbol{M}_D}{\partial\boldsymbol{u}_D} & \frac{\partial\boldsymbol{M}_D}{\partial\boldsymbol{\theta}_D}\end{bmatrix}_{\text{displaced}} = \begin{bmatrix}\boldsymbol{I} & \mathbf{0}\\ \tilde{\boldsymbol{s}}_\mathbf{0} & \boldsymbol{I}\end{bmatrix}\begin{bmatrix}\frac{\partial\boldsymbol{F}_S}{\partial\boldsymbol{u}_S} & \frac{\partial\boldsymbol{F}_S}{\partial\boldsymbol{\theta}_S}\\ \frac{\partial\boldsymbol{M}_S}{\partial\boldsymbol{u}_S} & \frac{\partial\boldsymbol{M}_S}{\partial\boldsymbol{\theta}_S}\end{bmatrix}\begin{bmatrix}\boldsymbol{I} & -\tilde{\boldsymbol{s}}_\mathbf{0}\\ \mathbf{0} & \boldsymbol{I}\end{bmatrix} + \begin{bmatrix}\mathbf{0} & \mathbf{0}\\ \mathbf{0} & \tilde{\boldsymbol{F}}_{S0}\tilde{\boldsymbol{s}}_\mathbf{0}\end{bmatrix} \tag{B23}$$

B2 Relationships at the displaced destination point for multiple source points

We now consider the case where multiple point sources are present. The derivation can be seen as a generalization of the previous case between two points, but special care is needed ~~,~~ when summing the contributions from the different nodes. The notations are illustrated in Figure B2. The loads at the destination points are obtained as:

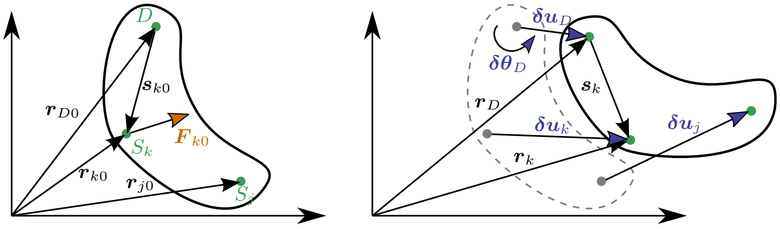

Figure B2. Rigid-body kinematics with the loads from multiple source points (S_j), transferred to a destination point (D)

$$\boldsymbol{F}_D = \sum_k \boldsymbol{F}_k \tag{B24}$$

$$\boldsymbol{M}_D = \sum_k \boldsymbol{M}_k + \tilde{\boldsymbol{s}}_{\boldsymbol{k}}\boldsymbol{F}_k \tag{B25}$$

where k is an index looping over all points of the rigid structure. To shorten notations, we define the vector between the destination point and a given point as:

$$\boldsymbol{s}_k = \boldsymbol{r}_k - \boldsymbol{r}_D \tag{B26}$$

$$\boldsymbol{s}_{k0} = \boldsymbol{r}_{k0} - \boldsymbol{r}_{D0} \tag{B27}$$

where $\boldsymbol{s}_k$ is the vector between the displaced points and $\boldsymbol{s}_{k0}$ is the vector prior to the displacement~~(at the operating condition).~~. Due to the rigid-body assumption, the elementary displacements of the points are related as follows:

$$\begin{aligned} \delta\boldsymbol{u}_D &= \delta\boldsymbol{u}_j + \tilde{\boldsymbol{s}}_{\boldsymbol{j0}}\delta\boldsymbol{\theta}_j \\ \delta\boldsymbol{\theta}_D &= \delta\boldsymbol{\theta}_j \end{aligned} \tag{B28}$$

from which one obtains the following ~~useful~~ relationships:

$$\frac{\partial\boldsymbol{u}_j}{\partial\boldsymbol{u}_D} = \boldsymbol{I}, \quad \frac{\partial\boldsymbol{\theta}_j}{\partial\boldsymbol{u}_D} = \boldsymbol{O}, \quad \frac{\partial\boldsymbol{u}_j}{\partial\boldsymbol{\theta}_D} = -\tilde{\boldsymbol{s}}_{\boldsymbol{j0}}, \quad \frac{\partial\boldsymbol{\theta}_j}{\partial\boldsymbol{\theta}_D} = \boldsymbol{I}, \quad \frac{\partial\boldsymbol{\theta}_j}{\partial\boldsymbol{\theta}_k} = \boldsymbol{I}\delta_{jk}, \quad \frac{\partial\boldsymbol{\theta}_j}{\partial\boldsymbol{u}_k} = \boldsymbol{O} \tag{B29}$$

Using a similar Taylor expansion as for the case with two nodes, the perturbation loads are obtained as:

$$\delta\boldsymbol{F}_D = \sum_k \delta\boldsymbol{F}_k \tag{B30}$$

$$\delta\boldsymbol{M}_D = \sum_k \delta\boldsymbol{M}_k + \tilde{\boldsymbol{s}}_{\boldsymbol{k0}}\delta\boldsymbol{F}_k + \tilde{\boldsymbol{F}}_{k0}(\tilde{\boldsymbol{s}}_{\boldsymbol{k0}}\delta\boldsymbol{\theta}_k) \tag{B31}$$

The chain rule for a given quantity of interest (Q) is obtained by summing over all the elementary variables:

$$dQ = \sum_j \frac{\partial Q}{\partial\boldsymbol{u}_j} d\boldsymbol{u}_j + \frac{\partial Q}{\partial\boldsymbol{\theta}_j} d\boldsymbol{\theta}_j \tag{B32}$$

For instance, ~~the application of the~~ applying the chain rule to $\boldsymbol{F}_D$ and using Equation B30 leads to:

$$\frac{\partial\boldsymbol{F}_D}{\partial\boldsymbol{u}_D} = \sum_j \frac{\partial\boldsymbol{F}_D}{\partial\boldsymbol{u}_j}\frac{\partial\boldsymbol{u}_j}{\partial\boldsymbol{u}_D} + \frac{\partial\boldsymbol{F}_D}{\partial\boldsymbol{\theta}_j}\frac{\partial\boldsymbol{\theta}_j}{\partial\boldsymbol{u}_D} = \sum_j\sum_k \frac{\partial\boldsymbol{F}_k}{\partial\boldsymbol{u}_j}\frac{\partial\boldsymbol{u}_j}{\partial\boldsymbol{u}_D} + \frac{\partial\boldsymbol{F}_k}{\partial\boldsymbol{\theta}_j}\frac{\partial\boldsymbol{\theta}_j}{\partial\boldsymbol{u}_D} = \sum_j\sum_k \frac{\partial\boldsymbol{F}_k}{\partial\boldsymbol{u}_j} \tag{B33}$$

Eventually, the Jacobians at the displaced destination node are obtained as:

$$\begin{bmatrix} \frac{\partial\boldsymbol{F}_D}{\partial\boldsymbol{u}_D} & \frac{\partial\boldsymbol{F}_D}{\partial\boldsymbol{\theta}_D} \\ \frac{\partial\boldsymbol{M}_D}{\partial\boldsymbol{u}_D} & \frac{\partial\boldsymbol{M}_D}{\partial\boldsymbol{\theta}_D} \end{bmatrix}_{\text{displaced}} = \sum_j \left\{ \sum_k \left(\begin{bmatrix} \boldsymbol{I} & \boldsymbol{0} \\ \tilde{\boldsymbol{s}}_{k0} & \boldsymbol{I} \end{bmatrix} \begin{bmatrix} \frac{\partial\boldsymbol{F}_k}{\partial\boldsymbol{u}_j} & \frac{\partial\boldsymbol{F}_k}{\partial\boldsymbol{\theta}_j} \\ \frac{\partial\boldsymbol{M}_k}{\partial\boldsymbol{u}_j} & \frac{\partial\boldsymbol{M}_k}{\partial\boldsymbol{\theta}_j} \end{bmatrix} \begin{bmatrix} \boldsymbol{I} & -\tilde{\boldsymbol{s}}_{j0} \\ \boldsymbol{0} & \boldsymbol{I} \end{bmatrix} \right) + \begin{bmatrix} \boldsymbol{0} & \boldsymbol{0} \\ \boldsymbol{0} & \tilde{\boldsymbol{F}}_{j0}\tilde{\boldsymbol{s}}_{j0} \end{bmatrix} \right\} \tag{B34}$$

Appendix C: Verification of the linear models

In this section, we supplement the results given in Section 3.3.3 ~~,~~ by showing free-decay results without hydrodynamics (no added mass, damping, hydrostatics). ~~We~~ In Figure C1, we show results with the structure only~~in~~, and results with the structure and moorings are reported in Figure C2. These results also include the nonlinear WELIB formulation. A strong agreement is found between the nonlinear OpenFAST and WELIB models, and between the linear OpenFAST and WELIB models. The yaw degree of freedom appears to be more challenging to capture for the linear models. We recall that OpenFAST and WELIB use different definition of the transformation matrices between the degrees of freedom, which results in different structural dynamic equations.

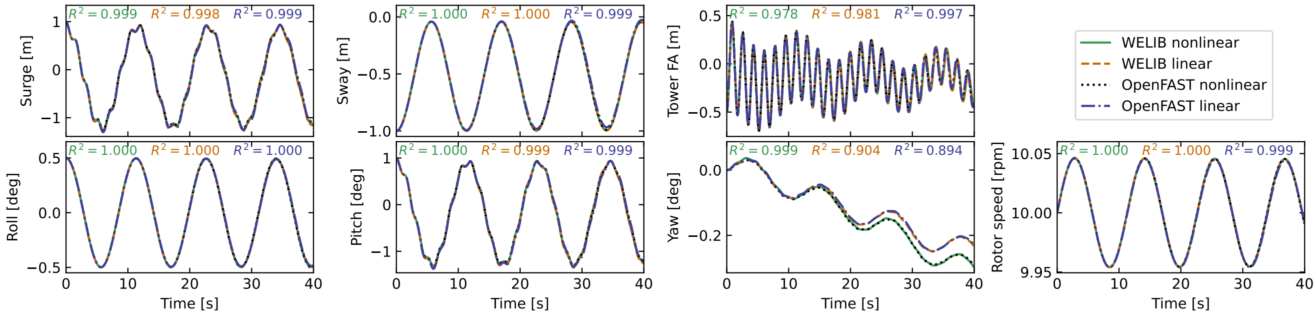

Figure C1. Free decay of the structure using nonlinear and linear models for a case including only the structure (no moorings, no hydrodynamics). Time series of the main ~~DOFs~~DOF.

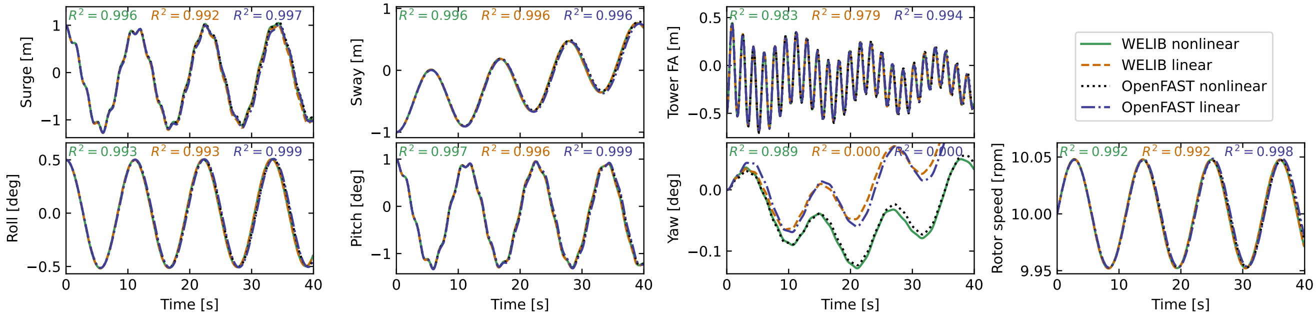

Figure C2. Free decay of the structure using nonlinear and linear models for a case including moorings (no hydrodynamics). Time series of the main ~~DOFs~~DOF.

Appendix D: Computation of section loads

In this section, we describe the nonlinear calculation procedure used in Section 3.6.2 to assess the section loads along the tower based on estimates of the structure kinematics and the loads at the tower top. For conciseness, in this appendix, we use x and z for the coordinates along the tower fore-aft and tower height, respectively, instead of x_T and z_T.

D1 Tower fore-aft bending moment and shear force

The fore-aft and side-side ~~loads are computed~~ moments are computed in the same way~~, therefore~~; therefore, this section focuses on the fore-aft direction. The sectional fore-aft bending moment at a given tower height z is determined as:

$$\mathcal{M}_y(z) = \mathcal{M}_{y,\text{top}} - \int_z^{L_T} S_x(z')dz' \tag{D1}$$

~~here~~ Here, $\mathcal{M}_{y,\text{top}}$ is the fore-aft bending moment at the tower top, and S_x is the shear force in the x direction, obtained as:

$$S_x(z) = \int_z^{L_T} p_{x,\text{all}}(z')\,dz' \tag{D2}$$

where $p_{x,\text{all}}$ is the force per unit length acting on the tower section in the fore-aft direction, including contributions from the external loads (aerodynamic loads on the structure), inertial loads due to the acceleration of the structure (including gravity), and nonlinear correction terms from the loads in the z direction ($p-\Delta$ effect, including self-weight effects). The different contributions are written as follows:

$$p_{x,\text{all}} = p_{x,\text{ext}} + p_{x,\text{corr}} - p_{x,\text{acc}} \tag{D3}$$

In this work, we neglect the external loads on the tower, $p_{x,\text{ext}} = 0$ (aerodynamic loads on the tower are typically small relative to rotor-thrust loads for an operating wind turbine). The acceleration contribution is $p_{x,\text{acc}} = -m(z)(a_{x,\text{struct}}(z) - a_{x,\text{grav}})$, where m is the mass per length along the beam, ~~and~~ $a_{x,\text{struct}}(z)$ is the acceleration of the section, determined based on the rigid-body acceleration of the floater and the elastic motion of the tower ($\dot{q}_T$ and $\ddot{q}_T$), and $a_{x,\text{grav}}$ is the acceleration of gravity in the x direction. The $p-\Delta$ correction term due to the vertical loading is computed as (see Branlard (2019)):

$$p_{x,\text{corr}} = \frac{d^2\Phi}{d^2z}\left[\int_z^L p_z\,dx' + \sum_{z_k \geq z} \mathcal{F}_{z,k}\right] - \frac{d\Phi}{dz}\left[p_z + \sum_k \mathcal{F}_{z,k}\delta(z - z_k)\right] \tag{D4}$$

where p_z is the vertical load per unit length (mostly consisting of the self-weight), $\mathcal{F}_{z,k}$ is the k~~-th~~th vertical force acting at point z_k, ~~and~~ δ is the Dirac function, and Φ is the shape function used to describe the tower displacement field (see Section 2.3.3). In our case, only the vertical force acting on top of the tower is present, $z_1 = L_T$ and $\mathcal{F}_{z,1} = \mathcal{F}_{z,\text{top}}$. The procedure ~~is similar~~ to compute the section loads in the y direction (using the $p-\Delta$ correction as well) is similar.

D2 Tower and ~~RNA~~ rotor-nacelle assembly kinematics

The determination of the tower section loads ~~require~~ requires a knowledge of the tower kinematics, to compute $\boldsymbol{a}_{\text{struct}}$, and ~~the RNA~~ of the rotor-nacelle assembly (RNA) kinematics, to compute the inertial contribution to the tower-top loads (see Section D3). The position, linear velocity, linear acceleration, rotational speed, and rotational acceleration of the floater (point F, body f) are given respectively by:

$$\boldsymbol{r}_F = \{x,y,z\}_i,\ \boldsymbol{v}_F = \{\dot{x},\dot{y},\dot{z}\}_i,\ \boldsymbol{a}_F = \{\ddot{x},\ddot{y},\ddot{z}\}_i, \tag{D5}$$

$$\boldsymbol{\omega}_f = \{\dot{\phi}_z,\dot{\phi}_y,\dot{\phi}_z\}_i,\ \dot{\boldsymbol{\omega}}_f = \{\ddot{\phi}_z,\ddot{\phi}_y,\ddot{\phi}_z\}_i \tag{D6}$$

where the notation i indicates that the coordinates of the vector are expressed in the inertial coordinate system. The transformation matrix from the floater to the inertial frame is obtained as ~~:~~ $\boldsymbol{R}_{f2i} = \boldsymbol{R}(\phi_x,\phi_y,\phi_z)$~~.~~, where $\boldsymbol{R}$ is a function computing the rotation matrix. The tower base (point T, body t) kinematics are obtained from the floater ~~using rigid body~~ motion using rigid-body kinematics:

$$\boldsymbol{r}_T = \boldsymbol{r}_F + \boldsymbol{r}_{FT}, \tag{D7}$$

$$\boldsymbol{v}_T = \boldsymbol{v}_F + \boldsymbol{\omega}_f \times \boldsymbol{r}_{FT}, \tag{D8}$$

$$\boldsymbol{a}_T = \boldsymbol{a}_F + \boldsymbol{\omega}_f \times (\boldsymbol{\omega}_f \times \boldsymbol{r}_{FT}) + \dot{\boldsymbol{\omega}}_f \times \boldsymbol{r}_{FT}, \tag{D9}$$

$$\boldsymbol{\omega}_t = \boldsymbol{\omega}_f, \quad \dot{\boldsymbol{\omega}}_t = \dot{\boldsymbol{\omega}}_f, \quad \boldsymbol{R}_{t2i} = \boldsymbol{R}_{f2i} \tag{D10}$$

where $\boldsymbol{r}_{FT}$ is the vector from the floater point to the tower base. The kinematics of a given tower section (point S, at height z) are given by:

$$\boldsymbol{r}_S = \boldsymbol{r}_T + \boldsymbol{r}_{TS} = \boldsymbol{r}_T + \boldsymbol{r}_{TS_0} + \boldsymbol{u}_S, \tag{D11}$$

$$\boldsymbol{v}_S = \boldsymbol{v}_T + \boldsymbol{\omega}_t \times \boldsymbol{r}_{TS} + \dot{\boldsymbol{u}}_S, \tag{D12}$$

$$\boldsymbol{a}_S = \boldsymbol{a}_T + \boldsymbol{\omega}_t \times (\boldsymbol{\omega}_t \times \boldsymbol{r}_{TS}) + \dot{\boldsymbol{\omega}}_t \times \boldsymbol{r}_{TS} + 2\omega_t \times \dot{\boldsymbol{u}}_S + \ddot{\boldsymbol{u}}_S, \tag{D13}$$

$$\boldsymbol{\omega}_s = \boldsymbol{\omega}_t + \boldsymbol{\omega}_{ts}, \tag{D14}$$

$$\dot{\boldsymbol{\omega}}_s = \dot{\boldsymbol{\omega}}_t + \dot{\boldsymbol{\omega}}_{ts} + \boldsymbol{\omega}_t \times \boldsymbol{\omega}_{ts}, \tag{D15}$$

where $\boldsymbol{r}_{TS_0} = z\hat{\boldsymbol{z}}_t$ is the vector from the tower base to the undeflected section, $\boldsymbol{u}_S$, $\dot{\boldsymbol{u}}_S$, $\ddot{\boldsymbol{u}}_S$ are the elastic motions of the section computed based on the shape function and the generalized coordinates, e.g., $\boldsymbol{u}_S(z) = \sum_j q_{t,j}\boldsymbol{\Phi}_j = q_t\Phi(z)\hat{\boldsymbol{x}}_t$ (see ~~e.g.,~~Branlard and Geisler (2022)). We note that OpenFAST also includes a vertical motion associated with the deflection (referred to as a "geometric nonlinearity")~~associated with the deflection~~, which we ~~are currently neglecting~~ neglect in this work. The transformation matrix from the section to the tower is $\boldsymbol{R}_{s2t} = \boldsymbol{R}(-u'_{S,y}, u'_{S,x}, 0)$, where $u_{S,y}$ and $u_{S,x}$ are the components of $\boldsymbol{u}_S$ in the tower coordinate system, and the prime notation indicates the differentiation with respect to z. The rotation speed and acceleration of the tower section with respect to the tower base are:

$$\boldsymbol{\omega}_{ts} = \left\{\dot{u}'_{S,y}, \dot{u}'_{S,x}, 0\right\}_t, \quad \dot{\boldsymbol{\omega}}_{ts} = \left\{\ddot{u}'_{S,y}, \ddot{u}'_{S,x}, 0\right\}_t \tag{D16}$$

The kinematics of the tower-top point and nacelle (point N, body n) are taken from the last section node (point S with $z = L_T$). Yawing, tilting, and rolling of the tower top would change the orientation matrix, rotational velocity, and rotational acceleration of the nacelle. These kinematics are omitted here for conciseness. The kinematics of the center of mass of the RNA (point G) are obtained using rigid-body kinematics~~(~~, identical to what was used between point F and T~~)~~.

D3 Tower-top loads

The tower-top loads are computed as follows:

$$\boldsymbol{\mathcal{F}}_{\text{top}} = \boldsymbol{\mathcal{F}}_{\text{aero}} - \boldsymbol{\mathcal{F}}_{\text{inertia}} \tag{D17}$$

$$\boldsymbol{\mathcal{M}}_{\text{top}} = \boldsymbol{\mathcal{M}}_{\text{aero}} - \boldsymbol{\mathcal{M}}_{\text{inertia}} \tag{D18}$$

where the aerodynamic loads are transferred to the tower top and where the inertial loads from the rigid-body RNA are:

$$\boldsymbol{\mathcal{F}}_{\text{inertia}} = M_{\text{RNA}}(\boldsymbol{a}_G - \boldsymbol{g}) \tag{D19}$$

$$\boldsymbol{\mathcal{M}}_{\text{inertia}} = \boldsymbol{r}_{NG} \times \boldsymbol{\mathcal{F}}_{\text{inertia}} + \boldsymbol{J}_G \cdot \dot{\boldsymbol{\omega}}_n + \boldsymbol{\omega}_n \times (\boldsymbol{J}_G \cdot \boldsymbol{\omega}_n) \tag{D20}$$

where: $\boldsymbol{r}_{NG}$ is the vector from the tower top to the center of mass of the RNA, M_{RNA} is the mass of the RNA, $\boldsymbol{J}_G$ is the inertia tensor of the RNA at it's center of mass, $\boldsymbol{a}_G$ is the linear acceleration of the center of mass of the RNA, $\boldsymbol{\omega}_n$ is the rotational acceleration of the RNA, and $\dot{\boldsymbol{\omega}}_n$ is the rotational acceleration of the nacelle. The load calculation is first done in the coordinate system of the nacelle ~~,~~and then transferred to the coordinate system of the tower where Equation D1 is defined.

References

Abbas, N., Zalkind, D., Pao, L., and Wright, A.: A Reference Open-Source Controller for Fixed and Floating Offshore Wind Turbines, Wind Energy Science Discussions, 2021, 1–33, https://doi.org/10.5194/wes-2021-19, 2021.

Auger, F., Hilairet, M., Guerrero, J. M., Monmasson, E., Orlowska-Kowalska, T., and Katsura, S.: Industrial Applications of the Kalman Filter: A Review, IEEE Transactions on Industrial Electronics, 60, 5458–5471, https://doi.org/10.1109/TIE.2012.2236994, 2013.

Bilbao, J., Lourens, E.-M., Schulze, A., and Ziegler, L.: Virtual sensing in an onshore wind turbine tower using a Gaussian process latent force model, Data-Centric Engineering, 3, https://doi.org/10.1017/dce.2022.38, 2022.

Bossanyi, E. A.: Individual Blade Pitch Control for Load Reduction, Wind Energy, 6, 119–128, https://doi.org/10.1002/we.76, 2003.

Bottasso, C. and Croce, A.: Cascading Kalman Observers of Structural Flexible and Wind States for Wind Turbine Control, Tech. rep., Dipartimento di Ingegneria Aerospaziale, Politecnico di Milano, Milano, Italy, Scientific Report DIA-SR 09-02, 2009.

Boukhezzar, B. and Siguerdidjane, H.: Nonlinear Control of a Variable-Speed Wind Turbine Using a Two-Mass Model, IEEE Transactions on Energy Conversion, 26, 149–162, https://doi.org/10.1109/TEC.2010.2090155, 2011.

Branlard, E.: Flexible multibody dynamics using joint coordinates and the Rayleigh-Ritz approximation: The general framework behind and beyond Flex, Wind Energy, 22, 877–893, https://doi.org/10.1002/we.2327, 2019.

Branlard, E.: wtDigiTwin GitHub repository https://github.com/NREL/wtDigiTwin https://doi.org/10.5281/zenodo.8048549 Last accessed June 2023, 2023a.

Branlard, E.: WELIB, Wind Energy Library, GitHub repository http://github.com/eBranlard/welib/, https://doi.org/10.5281/zenodo.8048349 Last accessed June 2023, 2023b.

Branlard, E. and Geisler, J.: A symbolic framework for flexible multibody systems applied to horizontal-axis wind turbines, Wind Energy Science, 2022.

Branlard, E., Giardina, D., and Brown, C. S. D.: Augmented Kalman filter with a reduced mechanical model to estimate tower loads on a land-based wind turbine: a step towards digital-twin simulations, Wind Energy Science, 5, 1155–1167, https://doi.org/10.5194/wes-5-1155-2020, 2020a.

Branlard, E., Jonkman, J., Dana, S., and Doubrawa, P.: A digital twin based on OpenFAST linearizations for real-time load and fatigue estimation of land-based turbines, Journal of Physics: Conference Series, 1618, 022 030, https://doi.org/10.1088/1742-6596/1618/2/022030, 2020b.

Castella, X. T.: Operations and maintenance costs for offshore wind farm analysis and strategies to reduce O&M costs, Master's thesis, Universitat Politècnica de Catalunya, and National Taiwan University of Science and Technology, 2020.

Cosack, N.: Fatigue Load Monitoring with Standard Wind Turbine Signals, Ph.D. thesis, Universität Stuttgart, 2010.

Dimitrov, N., Kelly, M. C., Vignaroli, A., and Berg, J.: From wind to loads: wind turbine site-specific load estimation with surrogate models trained on high-fidelity load databases, Wind Energy Science, 3, 767–790, https://doi.org/10.5194/wes-3-767-2018, 2018.

Eftekhar Azam, S., Chatzi, E., and Papadimitriou, C.: A dual Kalman filter approach for state estimation via output-only acceleration measurements, Mechanical Systems and Signal Processing, 60-61, 866 – 886, https://doi.org/https://doi.org/10.1016/j.ymssp.2015.02.001, 2015.

Evans, M., Han, T., and Shuchun, Z.: Development and validation of real time load estimator on Goldwind 6 MW wind turbine, Journal of Physics: Conference Series, 1037, 032 021, https://doi.org/10.1088/1742-6596/1037/3/032021, 2018.

Iliopoulos, A., Shirzadeh, R., Weijtjens, W., Guillaume, P., Hemelrijck, D. V., and Devriendt, C.: A modal decomposition and expansion approach for prediction of dynamic responses on a monopile offshore wind turbine using a limited number of vibration sensors, Mechanical Systems and Signal Processing, 68-69, 84–104, https://doi.org/https://doi.org/10.1016/j.ymssp.2015.07.016, 2016.

Jacquelin, E., Bennani, A., and Hamelin, P.: Force reconstruction: analysis and regularization of a deconvolution problem, Journal of Sound and Vibration, 265, 81 – 107, https://doi.org/https://doi.org/10.1016/S0022-460X(02)01441-4, 2003.

Jonkman, B. and Buhl, M.: TurbSim User's Guide, Tech. Rep. NREL/TP-500-39797, National Renewable Energy Laboratory, Golden, Colorado, USA, https://doi.org/10.2172/965520, 2006.

Jonkman, B., Mudafort, R. M., Platt, A., Branlard, E., Sprague, M., Jonkman, J., Vijayakumar, G., Buhl, M., Ross, H., Bortolotti, P., Masciola, M., Ananthan, S., Schmidt, M. J., Rood, J., Damiani, R., Mendoza, N., Hall, M., and Corniglion, R.: OpenFAST v3.4.1. Open-source wind turbine simulation tool, available at http://github.com/OpenFAST/OpenFAST/, https://doi.org/10.5281/zenodo.7632926, 2023.

Jonkman, J. M. and Jonkman, B. J.: FAST modularization framework for wind turbine simulation: full-system linearization, Journal of Physics: Conference Series, 753, 082 010, https://doi.org/10.1088/1742-6596/753/8/082010, 2016.

Jonkman, J. M., Wright, A. D., Hayman, G. J., and Robertson, A. N.: Full-System Linearization for Floating Offshore Wind Turbines in OpenFAST, vol. ASME 2018 1st International Offshore Wind Technical Conference of *International Conference on Offshore Mechanics and Arctic Engineering*, https://doi.org/10.1115/IOWTC2018-1025, v001T01A028, 2018.

Jonkman, J. M., Branlard, E., and Jasa, J. P.: Influence of wind turbine design parameters on linearized physics-based models in OpenFAST, Wind Energy Science, 7, 559–571, https://doi.org/10.5194/wes-7-559-2022, 2022.

Kalman, R. E.: A new approach to linear filtering and prediction problems, Journal of Basic Engineering, 12, 35–45, 1960.

Kamel, O., Kretschmer, M., Pfeifer, S., Luhmann, B., Hauptmann, S., and Bottasso, C.: Data-driven virtual sensor for online loads estimation of drivetrain of wind turbines, Forschung im Ingenieurwesen, pp. 1–8, https://doi.org/10.1007/s10010-023-00615-4, 2023.

Lourens, E., Reynders, E., Roeck, G. D., Degrande, G., and Lombaert, G.: An augmented Kalman filter for force identification in structural dynamics, Mechanical Systems and Signal Processing, 27, 446–460, 2012.

Ma, C.-K. and Ho, C.-C.: An inverse method for the estimation of input forces acting on non-linear structural systems, Journal of Sound and Vibration, 275, 953 – 971, https://doi.org/https://doi.org/10.1016/S0022-460X(03)00797-1, 2004.

Mehlan, F., R. Nejad, A., and Gao, Z.: Digital Twin Based Virtual Sensor for Online Fatigue Damage Monitoring in Offshore Wind Turbine Drivetrains, Journal of Offshore Mechanics and Arctic Engineering, 144, 1–9, https://doi.org/10.1115/1.4055551, 2022.

Mehlan, F., Keller, J., and R. Nejad, A.: Virtual sensing of wind turbine hub loads and drivetrain fatigue damage, Forschung im Ingenieurwesen, pp. 1–12, https://doi.org/10.1007/s10010-023-00627-0, 2023.

Mendez Reyes, H., Kanev, S., Doekemeijer, B., and van Wingerden, J.-W.: Validation of a lookup-table approach to modeling turbine fatigue loads in wind farms under active wake control, Wind Energy Science, 4, 549–561, https://doi.org/10.5194/wes-4-549-2019, 2019.

Noppe, N., Iliopoulos, A., Weijtjens, W., and Devriendt, C.: Full load estimation of an offshore wind turbine based on SCADA and accelerometer data, Journal of Physics: Conference Series, 753, 072 025, https://doi.org/10.1088/1742-6596/753/7/072025, 2016.

Schröder, L., Dimitrov, N. K., Verelst, D. R., and Sørensen, J. A.: Wind turbine site-specific load estimation using artificial neural networks calibrated by means of high-fidelity load simulations, Journal of Physics: Conference Series, 1037, 062 027, https://doi.org/10.1088/1742-6596/1037/6/062027, 2018.

Selvam, K., Kanev, S., van Wingerden, J. W., van Engelen, T., and Verhaegen, M.: Feedback–feedforward individual pitch control for wind turbine load reduction, International Journal of Robust and Nonlinear Control, 19, 72–91, https://doi.org/10.1002/rnc.1324, 2009.

Song, Z., Hackl, C., Anand, A., Thommessen, A., Petzschmann, J., Kamel, O., Braunbehrens, R., Kaifel, A., Roos, C., and Hauptmann, S.: Digital Twins for the Future Power System: An Overview and a Future Perspective, Sustainability, 15, 5259, https://doi.org/10.3390/su15065259, 2023.

Stiesdal Offshore: The TetraSpar full scale demonstration project, https://www.stiesdal.com/offshore-technologies/the-tetraspar-full-scale-demonstration-project/, 2022.

Zarchan, P. and Musoff, H.: Fundamentals of Kalman filtering : a practical approach, Fourth Edition, AIAA, Progress in astronautics and aeronautics, 2015.

Ziegler, L., Smolka, U., Cosack, N., and Muskulus, M.: Brief communication: Structural monitoring for lifetime extension of offshore wind monopiles: can strain measurements at one level tell us everything?, Wind Energy Science, 2, 469–476, https://doi.org/10.5194/wes-2-469-2017, 2017.